

# Generating An Advanced Cross-section Library For HTGR Pebble Bed Depletion Calculations Using Reduced-Order Model Generation Techniques

M3AT-24IN0601012

---

SEPTEMBER 2024

---

Yifeng Che,  
Olin W. Calvin,  
Yaqi Wang,  
Aadesh S. Deshmukh,  
Javier Ortensi,  
Paolo Balestra, and  
Gerhard Strydom

*Idaho National Laboratory*

Park, Hansol

*Argonne National Laboratory*



**DISCLAIMER**

This information was prepared as an account of work sponsored by an agency of the U.S. Government. Neither the U.S. Government nor any agency thereof, nor any of their employees, makes any warranty, expressed or implied, or assumes any legal liability or responsibility for the accuracy, completeness, or usefulness, of any information, apparatus, product, or process disclosed, or represents that its use would not infringe privately owned rights. References herein to any specific commercial product, process, or service by trade name, trade mark, manufacturer, or otherwise, does not necessarily constitute or imply its endorsement, recommendation, or favoring by the U.S. Government or any agency thereof. The views and opinions of authors expressed herein do not necessarily state or reflect those of the U.S. Government or any agency thereof.

# **Generating An Advanced Cross-section Library For HTGR Pebble Bed Depletion Calculations Using Reduced-Order Model Generation Techniques**

**M3AT-24IN0601012**

**Yifeng Che,  
Olin W. Calvin,  
Yaqi Wang,  
Aadesh S. Deshmukh,  
Javier Ortensi,  
Paolo Balestra, and  
Gerhard Strydom  
Idaho National Laboratory  
Park, Hansol  
Argonne National Laboratory**

**September 2024**

**Idaho National Laboratory  
INL ART Program  
Idaho Falls, Idaho 83415**

**<http://www.inl.gov>**

**Prepared for the  
U.S. Department of Energy  
Office of Nuclear Energy  
Under DOE Idaho Operations Office  
Contract DE-AC07-05ID14517**

*Page intentionally left blank*




## INL ART Program

# Generating An Advanced Cross-section Library For HTGR Pebble Bed Depletion Calculations Using Reduced-Order Model Generation Techniques

INL/RPT-24-80344

September 2024

**Technical Reviewer:** (Confirmation of mathematical accuracy, and correctness of data and appropriateness of assumptions.)



Mustafa Kamel Mohammad Jaradat  
Nuclear Engineer

8/28/2024

Date

**Approved by:**



Michael E. Davenport  
ART Project Manager

8/28/2024

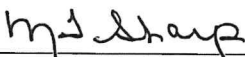
Date



Travis R. Mitchell  
ART Program Manager

8/28/2024

Date



Michelle T. Sharp  
INL Quality Assurance

8/28/2024

Date

*Page intentionally left blank*

## ABSTRACT

For code development, the Advanced Reactor Technologies Gas Cooled Reactors Program relies on a collaboration with the Nuclear Energy Advanced Modeling and Simulation Program, but the cross-sections generation and methodology definition is part of these program area goals. Based on previous studies in Fiscal Year 2023, the size of microscopic cross-section libraries increases rapidly with the number of tabulations, requiring a significant amount of memory and drastically slowing down the Griffin calculations when evaluating cross sections via the multivariate linear interpolation approach. Rising to these challenges, this work investigates constructing Reduced-order Models (ROMs) for the multigroup microscopic cross sections to accelerate the cross-section evaluation in Griffin. A database of multigroup cross sections is first collected considering all possible parameters designers could change during optimization studies. A downselection of various ROM techniques leads to Deep Neural Network (DNN) as the best candidate when jointly considering memory efficiency, predictive accuracy, computational cost, scalability, flexibility, and ease of implementation of the algorithms in comparison to multidimensional interpolation. This work develops a specific interface that enables cross-section predictions using pretrained DNN models in Griffin leveraging existing ROM capabilities. DNNs have been trained for all isotopes for use in Griffin. Preliminary Griffin testing shows that DNNs exhibit exceptional predictive accuracy, and the use of DNNs provides orders of magnitude of improvement in memory efficiency compared to conventional interpolation techniques. With such ROM techniques, it holds great promise to further increase the fidelity of the Pebble Bed Reactor (PBR) simulation by increasing the number of tabulations and state variables during cross-section evaluation, while keeping the computational cost affordable in Griffin.

*Page intentionally left blank*

# CONTENTS

ABSTRACT .....	v
ACRONYMS .....	xii
1. INTRODUCTION .....	1
1.1. Background and Motivation .....	1
1.2. Description of the Datasets .....	2
1.3. Characteristics of the Datasets .....	5
2. METHODOLOGY .....	7
2.1. Data Preprocessing and Organization .....	7
2.2. Reduced-Order Model Techniques .....	8
2.3. ROM Interface in Griffin .....	10
3. RESULTS .....	14
3.1. Downselection of ROM Techniques .....	14
3.2. DNN As the Selected ROM for All Isotopes .....	17
3.3. Griffin Testing .....	23
4. CONCLUSION .....	28
5. FUTURE WORK .....	28
6. REFERENCES .....	29
Appendix A. Additional Results for DNN Training .....	31
Appendix B. Complementary Results for Griffin Testing .....	32
B.1. Infinite Homogeneous Region of Three Isotopes .....	32
B.2. Infinite homogeneous region of 279 isotopes .....	39

## FIGURES

Figure 1.	Preliminary visualization of the self-shielded broad-group microscopic cross sections for representative isotopes. Different colors denote different energy groups, with neutron energy decreasing from the fast group ( $g_1$ ) to the thermal group ( $g_4$ ). . . . .	4
Figure 2.	Total number of pairwise relationships identified with strong linearity ( $ \rho  > 0.999$ ). . . . .	6
Figure 3.	Formulation of the input and output matrices for ROM training, using $^{235}\text{U}$ as a representative for the output matrix. . . . .	7
Figure 4.	Data flow of (a) cross-section generation and preparation and (b) evaluation in Griffin. Dashed green arrows describe the existing linear interpolation method, and the orange arrows explain the newly developed ROM technique in this work. . . . .	11
Figure 5.	Griffin implementation of the Torch and ISOXML interface. . . . .	14
Figure 6.	Comparison of the predictive accuracy of different Machine Learning (ML) algorithms for $^{235}\text{U}$ fission reaction. . . . .	15
Figure 7.	Prediction of the $^{235}\text{U}$ fundamental neutron reactions (except for the scattering matrix) on the <u>training</u> set. Each subfigure represents a different reaction. Predicted versus true values are shown for all nonzero energy groups, along with the R-squared ( $R^2$ ) and mean absolute percentage error (MAPE) metrics. . . . .	18
Figure 8.	Prediction of the $^{235}\text{U}$ fundamental neutron reactions (except for the scattering matrix) on the <u>test</u> set. Each subfigure represents a different reaction. Predicted versus true values are shown for all nonzero energy groups, along with the $R^2$ and MAPE metrics. . . . .	18
Figure 9.	Prediction of the $^{235}\text{U}$ scattering matrix on the <u>training</u> set. Predicted versus true values are shown for the nonzero entries in the scattering matrix, along with evaluation metrics, including $R^2$ , MAPE, root mean squared error (RMSE), and mean absolute error (MAE). . . . .	19
Figure 10.	Prediction of the $^{235}\text{U}$ scattering matrix on the <u>test</u> set. Predicted versus true values are shown for the nonzero entries in the scattering matrix, along with evaluation metrics, including $R^2$ , MAPE, RMSE, and MAE. . . . .	20
Figure 11.	Relative training error of DNNs for <u>fissionable</u> isotopes. For each isotope, the relative error is calculated as the mean relative error across all available reactions. Red lines represent data median. Blue boxes stand for the central 50% of data. Orange circles denote outliers falling out of the 25th/75th percentile. . . . .	21
Figure 12.	Comparison between DNN and multivariate linear interpolation on a uniform test grid for all reactions of $^{235}\text{U}$ . The central black dot marks the mean relative error. . . . .	22
Figure 13.	Simulated differences in reactivity between ISOXML data and DNN for a homogeneous region consisting $^{235}\text{U}$ , $^{238}\text{U}$ , and graphite at the burnup of (a) 0 GWd/tHM, (b) 39.6 GWd/tHM, (c) 79.2 GWd/tHM, (d) 118.8 GWd/tHM, (e) 158.4 GWd/tHM, and (f) 198.0 GWd/tHM. Blue bars stand for positive differences, and red ones for negative errors. . . . .	25
Figure 14.	Simulated differences in reactivity between ISOXML data and DNN for a homogeneous region consisting of 279 isotopes with number densities representative of a Middle of Life (MOL) fuel pebble in a PBR at the burnup of (a) 0 GWd/tHM, (b) 39.6 GWd/tHM, (c) 79.2 GWd/tHM, (d) 118.8 GWd/tHM, (e) 158.4 GWd/tHM, and (f) 198.0 GWd/tHM. Blue bars stand for positive differences, and red ones for negative errors. . . . .	26
Figure 15.	Simulated differences in the isothermal temperature coefficient of reactivity (ITC) between ISOXML data and DNN for a homogeneous region consisting of 279 isotopes with number densities representative of a MOL fuel pebble in a PBR at the burnup of (a) 0 GWd/tHM, (b) 39.6 GWd/tHM, (c) 79.2 GWd/tHM, (d) 118.8 GWd/tHM, (e) 158.4 GWd/tHM, and (f) 198.0 GWd/tHM. Blue bars stand for positive differences, and red ones for negative errors. . . . .	27

Figure 16. Relative training error of DNNs for <u>nonfissionable</u> isotopes. For each isotope, the relative error is calculated as the mean relative error across all available reactions. ....	31
Figure 17. Simulated differences in the macroscopic absorption rate between ISOXML data and DNN for a homogeneous region consisting of $^{235}\text{U}$ , $^{238}\text{U}$ , and graphite with number densities representative of a Beginning of Life (BOL) PBR fuel pebble at the burnup of (a) 0 GWd/tHM, (b) 39.6 GWd/tHM, (c) 79.2 GWd/tHM, (d) 118.8 GWd/tHM, (e) 158.4 GWd/tHM, and (f) 198.0 GWd/tHM. ....	33
Figure 18. Simulated differences in the macroscopic fission rate between ISOXML data and DNN for a homogeneous region consisting of $^{235}\text{U}$ , $^{238}\text{U}$ , and graphite with number densities representative of a BOL PBR fuel pebble at the burnup of (a) 0 GWd/tHM, (b) 39.6 GWd/tHM, (c) 79.2 GWd/tHM, (d) 118.8 GWd/tHM, (e) 158.4 GWd/tHM, and (f) 198.0 GWd/tHM.....	34
Figure 19. Simulated differences in the neutron flux in Energy Group 1 between ISOXML data and DNN for a homogeneous region consisting of $^{235}\text{U}$ , $^{238}\text{U}$ , and graphite with number densities representative of a BOL PBR fuel pebble at the burnup of (a) 0 GWd/tHM, (b) 39.6 GWd/tHM, (c) 79.2 GWd/tHM, (d) 118.8 GWd/tHM, (e) 158.4 GWd/tHM, and (f) 198.0 GWd/tHM.....	35
Figure 20. Simulated differences in the neutron flux in Energy Group 2 between ISOXML data and DNN for a homogeneous region consisting of $^{235}\text{U}$ , $^{238}\text{U}$ , and graphite with number densities representative of a BOL PBR fuel pebble at the burnup of (a) 0 GWd/tHM, (b) 39.6 GWd/tHM, (c) 79.2 GWd/tHM, (d) 118.8 GWd/tHM, (e) 158.4 GWd/tHM, and (f) 198.0 GWd/tHM.....	36
Figure 21. Simulated differences in the neutron flux in Energy Group 3 between ISOXML data and DNN for a homogeneous region consisting of $^{235}\text{U}$ , $^{238}\text{U}$ , and graphite with number densities representative of a BOL PBR fuel pebble at the burnup of (a) 0 GWd/tHM, (b) 39.6 GWd/tHM, (c) 79.2 GWd/tHM, (d) 118.8 GWd/tHM, (e) 158.4 GWd/tHM, and (f) 198.0 GWd/tHM.....	37
Figure 22. Simulated differences in the neutron flux in Energy Group 4 between ISOXML data and DNN for a homogeneous region consisting of $^{235}\text{U}$ , $^{238}\text{U}$ , and graphite with number densities representative of a BOL PBR fuel pebble at the burnup of (a) 0 GWd/tHM, (b) 39.6 GWd/tHM, (c) 79.2 GWd/tHM, (d) 118.8 GWd/tHM, (e) 158.4 GWd/tHM, and (f) 198.0 GWd/tHM.....	38
Figure 23. Simulated differences in the macroscopic absorption rate between ISOXML data and DNN for a homogeneous region consisting of 279 isotopes with number densities representative of a MOL PBR fuel pebble at the burnup of (a) 0 GWd/tHM, (b) 39.6 GWd/tHM, (c) 79.2 GWd/tHM, (d) 118.8 GWd/tHM, (e) 158.4 GWd/tHM, and (f) 198.0 GWd/tHM.....	43
Figure 24. Simulated differences in the macroscopic fission rate between ISOXML data and DNN for a homogeneous region consisting of 279 isotopes with number densities representative of a MOL PBR fuel pebble at the burnup of (a) 0 GWd/tHM, (b) 39.6 GWd/tHM, (c) 79.2 GWd/tHM, (d) 118.8 GWd/tHM, (e) 158.4 GWd/tHM, and (f) 198.0 GWd/tHM.....	44
Figure 25. Simulated differences in the fuel temperature coefficient of reactivity (FTC) between ISOXML data and DNN for a homogeneous region consisting of 279 isotopes with number densities representative of a MOL PBR fuel pebble at the burnup of (a) 0 GWd/tHM, (b) 39.6 GWd/tHM, (c) 79.2 GWd/tHM, (d) 118.8 GWd/tHM, (e) 158.4 GWd/tHM, and (f) 198.0 GWd/tHM.....	45

Figure 26. Simulated differences in the moderator temperature coefficient of reactivity (MTC) between ISOXML data and DNN for a homogeneous region consisting of 279 isotopes with number densities representative of a MOL PBR fuel pebble at the burnup of (a) 0 GWd/tHM, (b) 39.6 GWd/tHM, (c) 79.2 GWd/tHM, (d) 118.8 GWd/tHM, (e) 158.4 GWd/tHM, and (f) 198.0 GWd/tHM. ....	46
Figure 27. Simulated differences in the neutron flux for Energy Group 1 between ISOXML data and DNN for a homogeneous region consisting of 279 isotopes with number densities representative of a MOL PBR fuel pebble at the burnup of (a) 0 GWd/tHM, (b) 39.6 GWd/tHM, (c) 79.2 GWd/tHM, (d) 118.8 GWd/tHM, (e) 158.4 GWd/tHM, and (f) 198.0 GWd/tHM. ....	47
Figure 28. Simulated differences in the neutron flux for Energy Group 2 between ISOXML data and DNN for a homogeneous region consisting of 279 isotopes with number densities representative of a MOL PBR fuel pebble at the burnup of (a) 0 GWd/tHM, (b) 39.6 GWd/tHM, (c) 79.2 GWd/tHM, (d) 118.8 GWd/tHM, (e) 158.4 GWd/tHM, and (f) 198.0 GWd/tHM. ....	48
Figure 29. Simulated differences in the neutron flux for Energy Group 3 between ISOXML data and DNN for a homogeneous region consisting of 279 isotopes with number densities representative of a MOL PBR fuel pebble at the burnup of (a) 0 GWd/tHM, (b) 39.6 GWd/tHM, (c) 79.2 GWd/tHM, (d) 118.8 GWd/tHM, (e) 158.4 GWd/tHM, and (f) 198.0 GWd/tHM. ....	49
Figure 30. Simulated differences in the neutron flux for Energy Group 4 between ISOXML data and DNN for a homogeneous region consisting of 279 isotopes with number densities representative of a MOL PBR fuel pebble at the burnup of (a) 0 GWd/tHM, (b) 39.6 GWd/tHM, (c) 79.2 GWd/tHM, (d) 118.8 GWd/tHM, (e) 158.4 GWd/tHM, and (f) 198.0 GWd/tHM. ....	50



## TABLES

Table 1.	List of reactions, where “ng” denotes the number of energy groups. The reactions are identified as ”Basic,” (i.e., fundamental in nature) or ”Derived” (i.e., dependent on two or more fundamental reactions). . . . .	3
Table 2.	Control variables and tabulation points in the dataset. . . . .	3
Table 3.	ML algorithms considered for ROM construction. . . . .	9
Table 4.	Comprehensive performance comparison and downselection of ROM techniques in PyTorch. . . . .	16
Table 5.	DNN specification for each isotope. . . . .	17
Table 6.	Isotope densities used for Griffin 0D testing. . . . .	23
Table 7.	Summary of differences between the Torch model and the ISOXML model for the $^{235}\text{U}$ , $^{238}\text{U}$ , and graphite. All quantities are in units of per cent mille (pcm). . . . .	24
Table 8.	Summary of differences between the Torch model and the ISOXML model. . . . .	24
Table 9.	MOL PBR fuel pebble nuclide number densities. . . . .	39

*Page intentionally left blank*

## ACRONYMS

$R^2$	R-squared
ART	Advanced Reactor Technologies
BOL	Beginning of Life
CSR	Compressed Sparse Row
DFEM	Discontinuous Finite Element Method
DNN	Deep Neural Network
FE	Finite Element
FTC	fuel temperature coefficient of reactivity
GELU	Gaussian Error Linear Unit
GP	Gaussian Process Regression
HTGR	High-Temperature Gas-Cooled Reactor
IQR	Interquartile Range
ITC	isothermal temperature coefficient of reactivity
MAE	mean absolute error
MAPE	mean absolute percentage error
ML	Machine Learning
MOL	Middle of Life
MOOSE	Multiphysics Object-Oriented Simulation Environment
MSE	mean squared error
MTC	moderator temperature coefficient of reactivity

NEAMS	Nuclear Energy Advanced Modeling and Simulation
NN	Neural Network
OLS	Ordinary Least Squares
OP	overprediction
PBR	Pebble Bed Reactor
pcm	per cent mille
PLS	Partial Least Squares
PWR	Pressurized Water Reactor
RD	relative difference
RF	Random Forest
RMSE	root mean squared error
ROM	Reduced-order Model
SN	Discrete Ordinate
SVR	Support Vector Regression
UP	underprediction
XGB	EXtreme Gradient Boosting

*Page intentionally left blank*

# Generating an Advanced Cross-section Library for HTGR Pebble Bed Depletion Calculations Using Reduced-Order Model Generation Techniques

M3AT-24IN0601012

## 1. INTRODUCTION

### 1.1. Background And Motivation

Griffin is a reactor physics application built on the Multiphysics Object-Oriented Simulation Environment (MOOSE) framework. In the simulation of homogeneous and heterogeneous reactor dynamics, Griffin employs a Discontinuous Finite Element Method (DFEM) for solving the multigroup neutron transport equations. Such deterministic neutronics calculations rely on multigroup cross-section libraries, which are generated through either deterministic or Monte Carlo cross-section methods. The multigroup cross-section libraries used in Griffin typically comprise of either macroscopic or microscopic cross sections tabulated at discrete state points of various variables, e.g., burnup, moderator, and fuel temperature. These libraries are handled in Griffin by the ISOXML module with a native ISOXML format, containing comprehensive information for all required isotopes. During Griffin simulations, the microscopic cross sections, under desired conditions, are computed via multivariate linear interpolation. The microscopic cross sections and number densities are then used to calculate macroscopic cross sections. However, interpolating the microscopic cross sections raises computational challenges. On one hand, it mandates the generation and storage of substantial cross-section files, which may reach sizes as large as tens of gigabytes, leading to memory inefficiency. On the other hand, interpolating multidimensional data can be time-consuming, particularly with an increase in the number of tabulations in the ISOXML file. Compounding the issue is the fact that the microscopic cross-section libraries encompass information for all isotopes, numbering in hundreds for depletion calculations, each with its distinct set of reaction types and cross sections.

Facing these challenges, developing Reduced-order Models (ROMs) for neutron cross-section parameterization is an activate area of investigation. In [1], Deep Neural Networks (DNNs) were trained to predict the macroscopic resonance self-shielded cross-sections for Pressurized Water Reactor (PWR) applications. The adoption of DNN was concluded to be a promising way with high predictive accuracy and enhanced computational efficiency. In [2], DNNs were adopted to predict individual nodal parameters (nodal cross-sections, assembly discontinuity factors, etc.) for simulation of PWR 2D pin cell models. In this work, DNNs offered better flexibility and memory efficiency than traditional data functionalization methods. More recently, [3] demonstrated the use of artificial neural networks to predict macroscopic cross-sections. It was shown that the artificial neural networks can produce lower errors, i.e., better accuracy, relative to piece-wise linear models when the cross-sections exhibit nonlinear dependencies; especially when using coarse grid points. Artificial neural networks rendered a factor of two reduction in the errors. Nonetheless, for strongly linearly dependent cross-sections it was found that simpler linear regression outperforms deeper networks. The latest study in [4] used a combination of Principal Component Analysis and DNN as the ROM technique to approximate the multi-group cross-section libraries for dozens of isotopes and up to 50 energy groups. The employment of ROM in [4] demonstrated great computational efficiency and good predictive accuracy compared to directly using the XSPROC module from the NEWT code when simulating PWR assemblies. .

Driven by the current state of research, this study targets to develop ROMs that offer enhanced memory and predictive efficiency, to effectively mitigate the limitations associated with multidimensional interpolation. The initial part of this study involves visualizing and analyzing the pregenerated microscopic cross-section dataset, showcasing the linearity across different isotopes, reaction types, and broad-energy groups, henceforth

referred to as broad-groups. Secondly, the performance of classical Machine Learning (ML) algorithms is evaluated based on a combined assessment of predictive accuracy, prediction speed, training cost, memory efficiency, and scalability. DNNs are chosen ultimately for their superior prediction speed, memory efficiency, and scalability, despite some compromises in predictive accuracy and training cost. Finally, DNNs are trained for each isotope separately to predict all essential reaction types. DNNs are trained in PyTorch [5, 6] and loaded into Griffin through the PyTorch C++ API, LibTorch [7], to predict the microscopic cross sections when solving the neutron transport equations, in replacement of interpolation based on the ISOXML-formatted file. Preliminary Griffin testing has shown a clear advantage of the ROM techniques, especially in memory efficiency, and more rigorous testings will be performed in Griffin as part of the ongoing work jointly under the Advanced Reactor Technologies (ART) Program and the Nuclear Energy Advanced Modeling and Simulation (NEAMS) Program.

## 1.2. Description Of The Datasets

Broad-group self-shielded microscopic cross-section data for all isotopes and corresponding reactions is initially generated using the lattice physics code DRAGON5 [8] from a one-dimensional High-Temperature Gas-Cooled Reactor (HTGR) pebble problem. Table 1 shows the possible reaction types in the pregenerated dataset. As a simplest demonstration, the control variables include *burnup* (average burnup), *tmod* (moderator temperature), and *tfuel* (fuel temperature). The self-shielded microscopic cross-section dataset is generated on a uniform grid, with physical ranges and the number of tabulation points described in Table 2 for each control variable, respectively. In this study, the dataset comprises information for 295 isotopes, with cross-section information condensed into four broad-groups. The broad-group boundaries are  $[1.96403 \times 10^7, 1.95066 \times 10^5, 17.5648, 2.33006, 1.10003 \times 10^{-4}]$  eV from the highest to lowest energy groups, and the number of delayed neutron groups is six. This broad-group structure is adapted from the four-group structure detailed in [9] for Fort St. Vrain, with slight modifications to the boundaries to align with the 361-group fine structure available in DRAGON5 [8]. The choice of broad-group structure is important since it can affect the efficacy of the techniques included in this work, i.e., microscopic cross-sections can exhibit highly nonlinear, oscillatory behavior near resonance structures, which could lead to large errors in predictive capability of reduced order models. Thinning is applied to the grid data to reduce the data file size, i.e., every other tabulation point is retained for the training set, while every third tabulation point is selected for the test set. Downselection of the ROM in Section 3.1 is based on a training set containing 5,184 samples (occupying 1.52 GB on a local disk) and another test containing 1,367 samples spanning the same parameter ranges with no overlap with the training set. The final ROM training in Section 3.2 employs the full dataset that consists of 19,529 training samples (occupying 11.13 GB on a local disk).

The pregenerated multigroup cross-section dataset (all 5,184 samples) is visualized for a few representative isotopes, as shown in Figure 1. Neutron energy decreases progressively from the fast group (NG-1) to the thermal group (NG-4), and different energy groups are distinguished by colors. Cross sections in different energy groups can vary by orders of magnitude, with only some showing a clear dependence on certain control variables. At a given x-axis point, the data span within the same color represent variation of the cross-section values due to perturbation of the other two control variables in a specific energy group. A wider variation band indicates larger sensitivity of the cross section to other two control variables. For example,  $^{235}\text{U}$  has the largest fission cross sections in the thermal group (NG-4), exhibiting a strong dependence on both burnup and moderator temperature. Fissile isotopes like  $^{235}\text{U}$  and  $^{239}\text{Pu}$  present large fission cross sections (hundreds of barns) in the thermal group. On the contrary, the fission cross section of  $^{238}\text{U}$  and  $^{240}\text{Pu}$  are two orders of magnitude smaller than that for  $^{235}\text{U}$  and  $^{239}\text{Pu}$ , exhibiting weak dependence on the state variables.

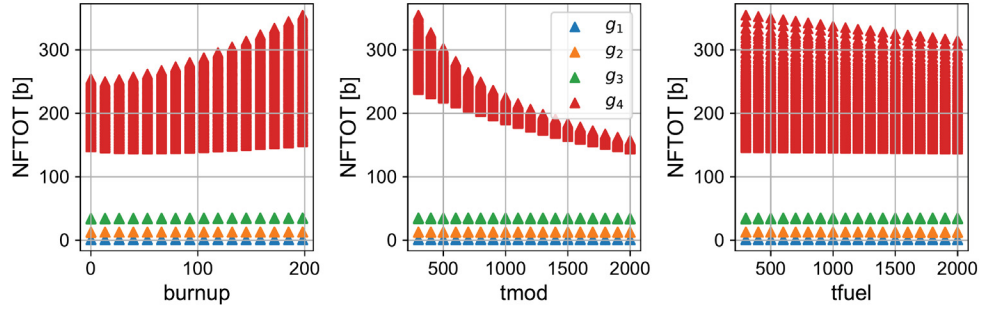
Table 1. List of reactions, where “ng” denotes the number of energy groups. The reactions are identified as ”Basic,” (i.e., fundamental in nature) or ”Derived” (i.e., dependent on two or more fundamental reactions).

Reaction	DRAGON Name	Definition	Note	Size
$\sigma_f$	NFTOT	Fission	Basic	(ng)
$\nu\sigma_f$	NUSIGF	Neutron production from fission	Derived	(ng)
$\kappa\sigma_f$	H-FACTOR	Energy production from fission	Basic	(ng)
$\Sigma_s$	SCATRD	Neutron scattering production matrix	Basic	(ng, ng)
$\chi_p$	CHI	Prompt neutron spectrum	Basic	(ng)
$\sigma_{n,\gamma}$	NG	Radiative capture	Basic	(ng)
$\sigma_a$	ABS	Absorption	Derived	(ng)
$\sigma_r$	REM	Removal	Derived	(ng)
$\sigma_t$	STRD	Total	Derived	(ng)
$\sigma_{n,2n}$	N2N	$2n$ production	Basic	(ng)
$\sigma_{n,3n}$	N3N	$3n$ production	Basic	(ng)
$\sigma_{n,4n}$	N4N	$4n$ Production	Basic	(ng)
$\sigma_{n,p}$	NP	Proton production	Basic	(ng)
$\sigma_{n,d}$	ND	Deuteron production	Basic	(ng)
$\sigma_{n,t}$	NT	Triton production	Basic	(ng)
$\sigma_{n,np}$	NNP	$n + p$ production	Basic	(ng)
$\sigma_{n,\alpha}$	NA	$\alpha$ production	Basic	(ng)
$\sigma_{n,2\alpha}$	N2A	$2\alpha$ production	Basic	(ng)

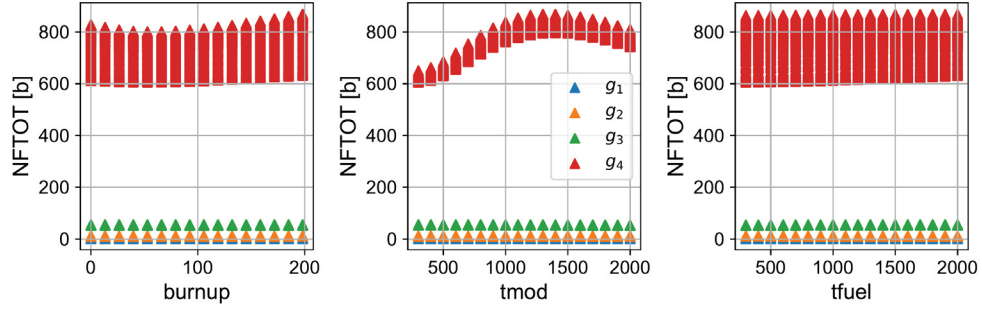
Table 2. Control variables and tabulation points in the dataset.

Control Variables	Unit	Physical Range	Number of Tabulations Points
burnup	GWd/tHM	[0, 198]	31
tmod	K	[300, 2000]	35
tfuel	K	[300, 2000]	35

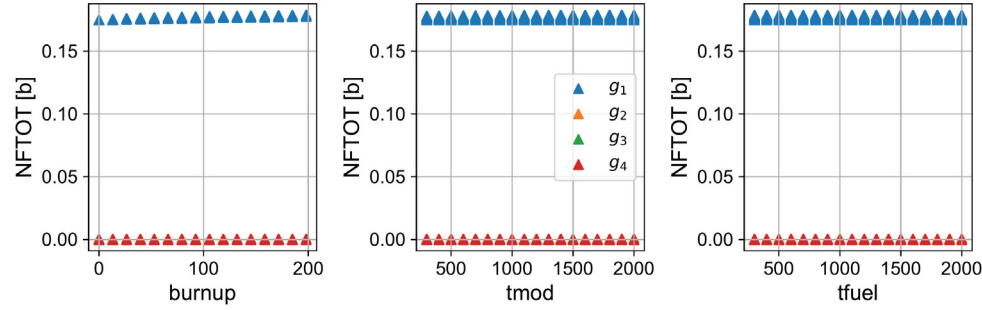




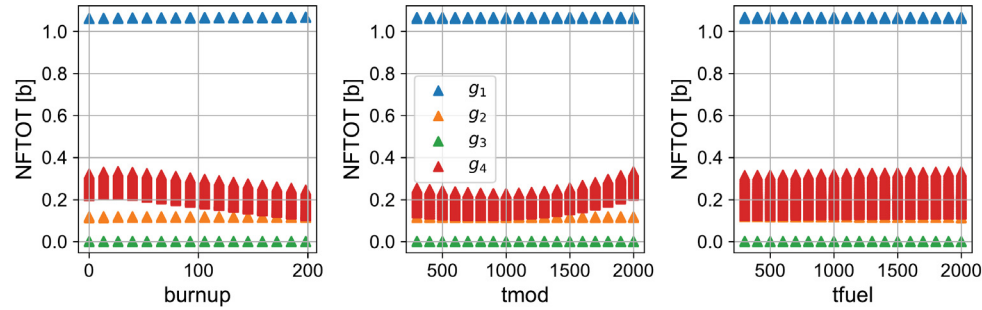
(a) Fission cross section for  $^{235}\text{U}$



(b) Fission cross section for  $^{239}\text{Pu}$



(c) Fission cross section for  $^{238}\text{U}$



(d) Fission cross section for  $^{240}\text{Pu}$

Figure 1. Preliminary visualization of the self-shielded broad-group microscopic cross sections for representative isotopes. Different colors denote different energy groups, with neutron energy decreasing from the fast group ( $g_1$ ) to the thermal group ( $g_4$ ).

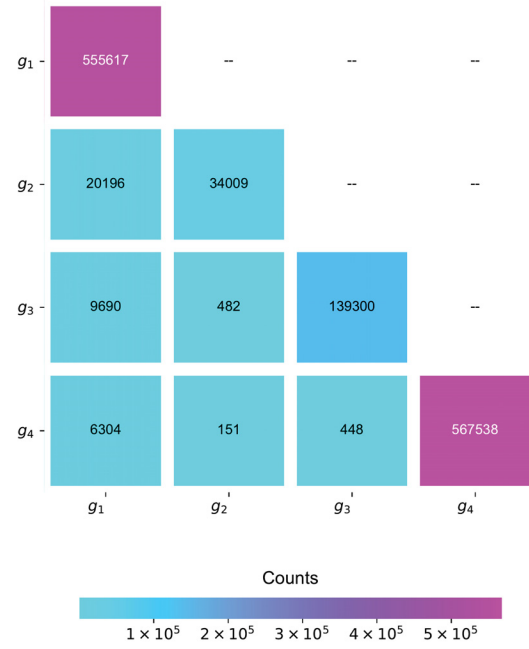
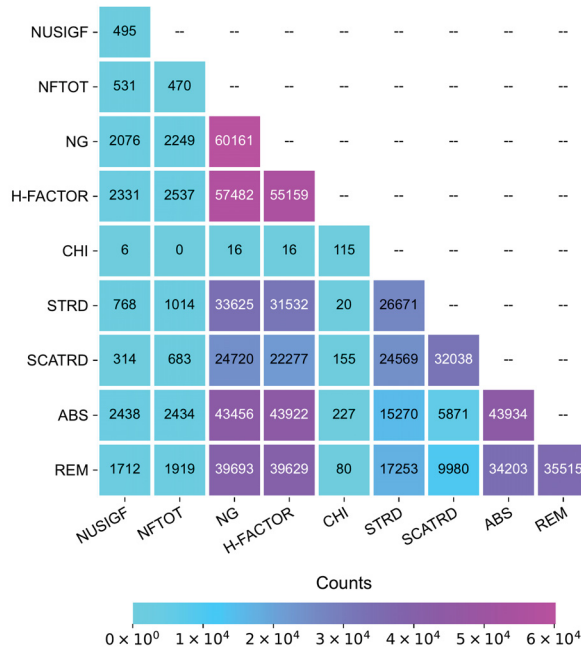
### 1.3. Characteristics Of The Datasets

This section presents a correlation analysis to identify potential linear relationships in cross-section data across all isotopes, reaction types, and energy groups. The Pearson correlation coefficient  $\rho$ , which is a common measure of linear correlation, is calculated pairwise for the cross section of a specific isotope, reaction type, and energy group following Equation 1:

$$\rho = \frac{\text{Cov}(X, Y)}{\sigma_X \sigma_Y} = \frac{\mathbb{E}[XY] - \mathbb{E}[X]\mathbb{E}[Y]}{\sqrt{\mathbb{E}[X^2] - (\mathbb{E}[X])^2} \sqrt{\mathbb{E}[Y^2] - (\mathbb{E}[Y])^2}} \quad (1)$$

where  $X$  and  $Y$  represent the two variables to analyze and  $\rho$  is a number between -1 and +1, with  $\rho > 0$  meaning a positive correlation,  $\rho < 0$  indicating a negative correlation, and  $\rho = 0$  showing no relationship between the two variables.

The Pearson correlation coefficient is analyzed for all isotopes, reaction types, and energy groups. The total number of pairwise relationships with strong linearity ( $|\rho| > 0.999$ ) is shown for essential reaction types across all isotopes and all energy groups, as shown in Figure 2. Note that threshold reactions like N2N, N3N, N4N, etc. are excluded from this correlation analysis. Linearity within the same reaction type (diagonal entries in Figure 2(a)) is expected, as isotopes with similar properties tend to exhibit similar behavior. The off-diagonals, denoting similarities across reaction types, need to be interpreted carefully, as strong linearity fundamentally exists among derived reaction types. For example, NFTOT ( $\sigma_f$ ), NUSIGF ( $\nu\sigma_f$ ), and H-FACTOR ( $\kappa\sigma_f$ ) are correlated through  $\sigma_f$ ; the removal cross section (REM) is derived from both total cross section (STRD) and the self-scattering terms in the scattering matrix (SCATRD); and the absorption cross section (ABS) is related to the gamma radiative capture (NG) and other nonscattering neutron interactions. Other than that, a high linear relationship presents across reaction types (e.g., between STRD and NG, STRD and H-FACTOR, SCATRD and NG, SCATRD and H-FACTOR, NG and H-FACTOR, etc.). Similarly, Figure 2(b) shows the Pearson coefficients analyzed for the four energy groups compressing information across all isotopes and all reaction types. The results show that strong correlation among the cross section data in different energy groups widely exist, despite the fact that the majority of such correlation stays within the same energy group. The correlation analysis reveals the linear dependency in the dataset, spanning isotopes, reaction types, and energy groups. This indicates the potential for dimensionality reduction, which could simplify the process of surrogate construction. However, such linear dependency can vary significantly across different isotopes, necessitating detailed analysis and documentation. As a compromise, we construct a separate surrogate model for each isotope, capable of predicting all associated reactions in all energy groups, as will be demonstrated in the following sections.



(a) Pearson coefficients  $\rho$  between reactions across all isotopes, all energy groups

(b) Pearson coefficients  $\rho$  between energy groups across all isotopes, all reactions

Figure 2. Total number of pairwise relationships identified with strong linearity ( $|\rho| > 0.999$ ).

## 2. METHODOLOGY

### 2.1. Data Preprocessing And Organization

Input to the ROMs contains three state variables ( $burnup$ ,  $t_{mod}$ , and  $t_{fuel}$ ) as described in Table 2. Assuming the distinct combinations of these three state variables to be  $N$ , the shape of the input matrix is therefore  $(N, 3)$ . The formulation of the output matrix needs to be discussed separately for two different scenarios. For downselecting the ROM techniques, as will be presented in Section 3.1, the output matrix is formulated to contain all energy groups of a specific reaction of a designated isotope. Each row contains all four energy groups of a reaction (with the exception being the scattering production matrix, for which we predict the *nonzero* entries in the lower triangular matrix), and the total number of rows is the same as that for the input matrix. For practical ROM generation to support the Griffin simulations, a ROM will be produced for each isotope to predict all the *basic* reactions. Note that each isotope is associated with a unique set of reactions, so the total number of reactions  $N_R$  varies for different isotopes. For each state, the cross-section data is flattened and concatenated into a long row vector of size  $N_{output}$ , so the corresponding output matrix is  $(N, N_{output})$ .

Figure 3 gives a more detailed explanation of the input and output matrix organization. In this work, as described in Section 2, the training set contains 5,184 samples and the test set contains 1,367 samples. Correspondingly, shape of the input matrices are  $(5,184, 3)$  and  $(1,367, 3)$  for the training and test set, respectively. The dimension of the output matrix may vary for different isotopes, and Figure 3 shows the information for  $^{235}\text{U}$  as an illustration. For  $^{235}\text{U}$ , basic reactions that need be predicted are [NG, N2N, N3N, N4N, H-FACTOR, NFTOT, CHI, NUSIGF, SCATRD], as shown in the “DRAGON5 Name” column in Table 1. Each one of the NG (N-Gamma), H-FACTOR (fission energy production), NFTOT (fission), CHI (prompt neutron spectrum), and NUSIGF (neutron production from fission) contains information for all four energy groups. Therefore, the first four columns in the output matrix represent the first, second, third and fourth energy group for the N-Gamma reaction respectively, and similarly for other quantities.

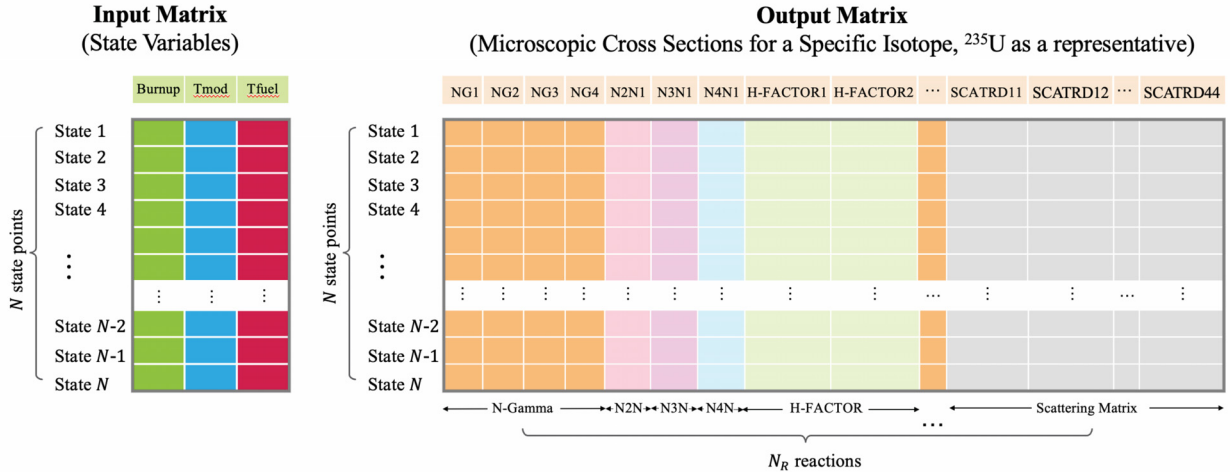


Figure 3. Formulation of the input and output matrices for ROM training, using  $^{235}\text{U}$  as a representative for the output matrix.

It is noteworthy that some nonscattering neutron interactions, such as [N2N, N3N, N4N], are *threshold reactions* that only occur above a certain energy threshold. In other words, a large amount of imbalanced mixed-zeros data exist for these reactions. In this work, broad-groups containing all-zero data are dropped

off the output matrix for two reasons. First, most ML algorithms struggle when predicting imbalanced mixed-zeros data during regression. Second, predetermination of the all-zero entries in these threshold reactions can be easily achieved by comparing the threshold energy and the broad-group boundaries. Therefore, the output matrix for  $^{235}\text{U}$  only contains the first energy group for these threshold reactions (i.e., N2N1, N3N1, and N4N1) as these reactions are only activated at the fast spectrum.

The neutron scattering production matrix SCATRD ( $\Sigma_{s,g \rightarrow g'}$ ) essentially represents how neutrons scatter from one energy group ( $g$ ) to another ( $g'$ ). Furthermore, it includes neutron production terms from (n,xn) reactions in the main diagonal; typically in the higher energy range. Theoretically, the shape of the full scattering production matrix is  $(ng, ng)$ . Practically, most neutrons are *downscattered* from a higher energy  $g$  group to a lower energy group  $g'$  (where  $g > g'$ ) or self-scatter (where  $g = g'$ ). The downscattering cross section can be zero in specific energy groups, for example,  $\Sigma_{s,2 \rightarrow 4} = 0$  for  $^{235}\text{U}$  when using the aforementioned  $ng = 4$  energy group structure. Moreover, *upscattering* where neutrons gain energy during a scatter event thus moving from a lower energy group  $g$  to a higher energy group  $g'$  (where  $g < g'$ ) can also occur, especially near the thermal spectrum ( $\Sigma_{s,4 \rightarrow 3} \neq 0$  for  $^{235}\text{U}$  as an example). Although the upscattering cross section is usually orders of magnitude smaller than the self-scattering terms, it is still essential to predict this term in order to accurately track neutron interactions. In summary, the scattering production matrix describes the unique neutron scattering properties of each isotope, and often deviates from a perfect triangular matrix. In this work, we adopted the Compressed Sparse Row (CSR) [10] representation of the scattering matrix. All nonzero entries in the scattering matrix are concatenated to the end of the output matrix, as shown in Figure 3. For  $^{235}\text{U}$ , entries of the scattering matrix being predicted are [SCATRD-11, SCATRD-12, SCATRD-22, SCATRD-13, SCATRD-23, SCATRD-33, SCATRD-43, SCATRD-14, SCATRD-34, SCATRD-44], with SCATRD-34 being the upscattering term and SCATRD-24 missing as it is all zero.

Finally, both input and output data are normalized by a *NormalScaler*, which subtracts the mean of training samples and scales to unit variance before feeding into the ROMs. It is noteworthy that this work observed larger maximum absolute predictive errors when using *MinMaxScalers*, which transforms features by subtracting the minimum value then dividing by the range of the feature. Therefore, the *NormalScaler* is consistently used hereinafter.

## 2.2. Reduced-Order Model Techniques

Given that the primary challenges with multivariate interpolation are the high memory requirements and low computational efficiency as the number of control variables increases, our investigation into the feasibility of different ROM techniques has prioritized memory efficiency and model scalability, in addition to ensuring good predictive accuracy and speed. As a preliminary downselection of the ROM techniques, four major types of ML algorithms are considered, as listed in Table 3:

1. **Linear regression.** Linear regression is a popular choice due to its simplicity, interpretability, and efficiency. Moreover, variants of linear regression methods can capture nonlinear relationships between variables, enhancing their expressiveness while retaining the original advantages. This work employs Partial Least Squares (PLS) regression [11] that projects both predicted and observable variables to a latent space, in addition to polynomial transformation of the input variables as a feature engineering technique on top of an Ordinary Least Squares (OLS) linear regression.
2. **Kernel methods.** Kernel methods [12] employ kernel functions to provide an efficient similarity measure in a high-dimensional, implicit feature space, which is often computationally cheaper than the explicit calculation of the dependent variables. This work selects two of the most popular kernel methods, Support Vector Regression (SVR) [13] and Gaussian Process Regression (GP) [14] for demonstration purposes.

3. **Tree-based algorithms.** Tree-based algorithms are another type of powerful ML algorithms with high accuracy, stability, and ease of interpretation when mapping nonlinear relationships for regression problems. This work utilizes Random Forest (RF) [15] and EXtreme Gradient Boosting (XGB) [16] as two representative methods.
4. **Neural Network (NN).** Finally, DNNs are also employed in this work for its superior flexibility, scalability, and most importantly, its nature of being a universal function approximator [17].

Table 3. ML algorithms considered for ROM construction.

Category	Notation	Name
Linear Regression	PLS	Partial Least Squares Regression
	OLS-Poly	Ordinary Least Squares (with polynomial features)
Kernel-Based Methods	SVR	Support Vector Regression
	GP	Gaussian Process
Tree-Based Algorithms	RF	Random Forest
	XGB	eXtreme Gradient Boosting
Neural Networks	DNN	Deep Neural Networks

Practically, many ML methods could achieve similarly good precision when properly tuned on the same dataset. It is therefore essential to consider other constraints posed by our microscopic multigroup cross-section problem, which requires a large number of cross-section evaluations at each spatial location, at each linear and nonlinear Finite Element (FE) solve for each isotope. Downselection of the ROM techniques in this work is based on a comprehensive consideration of the following criteria:

- (a) **Accuracy:** The constructed ROM should give accurate predictions not only on the training set, but also on unseen data. To ensure good predictive accuracy across all physical ranges, it is essential to collect high-quality training data that sufficiently and uniformly covers the entire physical domain. Metrics such as mean absolute error (MAE), root mean squared error (RMSE), and R-squared ( $R^2$ ) are used to evaluate the accuracy of the trained model on both training and test sets. Independent high-quality training and test sets that sufficiently cover possible physical ranges need be collected to select the right model architecture and avoid overfitting and underfitting. The ROM prediction is expected to be as accurate as the multivariate linear interpolation to avoid error accumulation in practical Griffin simulations.
- (b) **Memory efficiency:** Memory efficiency is another crucial factor, especially when working with large microscopic cross-section datasets and deploying models in resource-constrained environments like Griffin and MOOSE. Contrary to the multivariate linear interpolation approach which requires loading in the full microscopic cross-section library that can be tens of gigabytes in size, the ROM is expected to consume much less memory during the whole process of data preprocessing, training, and evaluation.
- (c) **Speed:** The computational cost associated with model training, retraining, and evaluation is essential when selecting the appropriate ROM technique. Given that the interpolation method does not involve any training procedure, the training cost of a ROM should not be burdensome. Moreover, retraining the ROM should be relatively easy, as the model might need be periodically retrained upon the availability of more high-quality data, or when the reactor moves away from the original conditions used to generate the training set. More importantly, the computational cost for a ROM evaluation should be cheaper or at most comparable to that of the interpolation method, as Griffin simulations require a large number of microscopic cross-section evaluations for hundreds of isotopes at multiple locations at each time



step. Assuming the number of state variables being  $d$  and the number of grid points in each dimension being  $n$ , the cost of grid-based multivariate linear interpolation is  $\mathcal{O}(d \log(n) + 2^d)$  [18], which is used as a benchmark in this work to evaluate the ROM performance.

- (d) **Scalability:** Scalability of the model is another key factor when selecting ROM methods. This refers to the capability of a model to scale to high dimensionality or an enormous amount of data without compromising on performance or precision. Although the current work is demonstrated on a simple dataset with only three state variables, the self-shielded cross-section dataset will be extended to consider more state variables, which will result in an increase of the input dimensionality. Moreover, for integrating the ROM training with online cross-section generation in Griffin, scalability of the ROM to a large training set becomes a key selection criteria.
- (e) **Robustness:** Another factor to consider is the model robustness to adversarial and noisy conditions and different regimes. This in general requires a wise choice of regularization techniques, loss functions, optimization algorithms, cross validation, potential employment of ensemble methods, etc.
- (f) **Implementation:** Lastly, it is essential to ensure the choice of ROM technique is compatible with the MOOSE framework, ideally taking advantage of existing interfaces with the MOOSE framework.

A detailed comparison of different ROM techniques will be presented in Section 3.1. It will be shown that DNNs outperform other techniques when jointly considering all the above aspects. Moreover, as will be described in Section 2.3, interfacing a DNN with MOOSE and Griffin is easy when leveraging the existing LibTorch interface [7] in MOOSE. Therefore, this work trains a DNN to predict all reactions for each isotope.

## 2.3. ROM Interface In Griffin

One advantage of choosing DNNs as the ROM technique is that we can build upon the existing LibTorch API [7] that has been integrated and tested under the MOOSE framework. Figure 4 describes the data flow of cross-section generation in DRAGON5, preparation in Python, and evaluation in Griffin, comparing the conventional ISOXML approach and the newly developed ROM method. Initially, deterministic neutron cross sections are generated in DRAGON5 on a predetermined uniform parameter grid. With the conventional approach, the tabulated cross-section data are organized into an ISOXML (*.xml*) format that is typically gigabytes in size when containing the information for all isotopes. Then the ISOXML file is loaded into Griffin, and the cross sections are evaluated via multivariate linear interpolation. With the ROM technique developed in this work, DNNs are trained based on the pregenerated DRAGON5 dataset. Then the process of model training and selection is conducted in PyTorch, and the trained DNN model is serialized into a LibTorch readable format (*.pt* file). One *.pt* file is produced for each isotope, and a JSON descriptor (*.json* file) depicting properties of the Torch models, input and output normalization, etc. is produced for all isotopes, as will be detailed next. Eventually, the ROM-assisted cross-section evaluation will be compared against the ISOXML approach by examining the difference in simulated reactivity, neutron fluxes, etc.

Switching from the ISOXML file to the Torch model plus JSON descriptor induces a series of syntax changes. As an example, Listing 1 shows the ISOXML syntax for  $^{235}\text{U}$ . The *.xml* file stores the tabulated cross-section data for all necessary neutron reactions, such as NGamma, N2N, N3N, etc. Table `gridIndex` indicates a specific combination of the *burnup*, *tmod* and *tfuel* indices, and the *.xml* file iterates over all states of *burnup*, *tmod*, and *tfuel* to formulate a tabulated data matrix in Griffin. The resulting ISOXML file is therefore bulky, especially when considering large number of isotopes or increased tabulation points. The JSON file, on the contrary, is much lighter in content. As evidenced in Listing 2, which shows the JSON syntax for  $^{235}\text{U}$ , below is a detailed explanation for each entry in the JSON file:

- `name` denotes the isotope name.

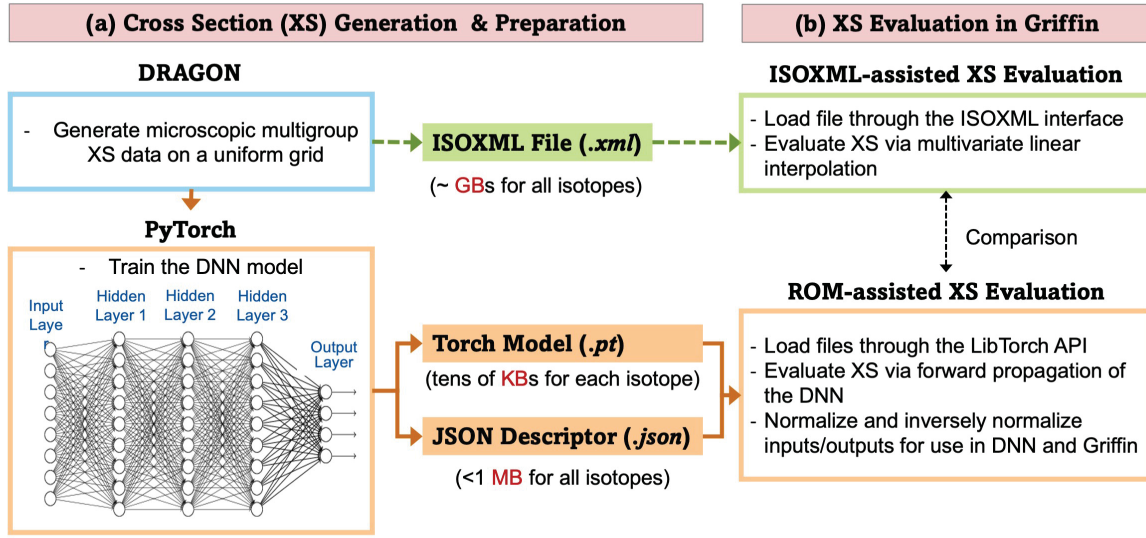


Figure 4. Data flow of (a) cross-section generation and preparation and (b) evaluation in Griffin. Dashed green arrows describe the existing linear interpolation method, and the orange arrows explain the newly developed ROM technique in this work.

- `material_id` represents a unique cross-section region of interest in Griffin simulation.
- `model_path` points to the location of the torch model.
- `variables` describes the state variables being considered during cross-section generation.
- `variable_scaling` stores the mean and standard deviation of the input state variables.
- `reactions` lists all neuron reactions being predicted by the Torch model.
- `indices` entries under each reaction type denotes the index in the DNN output using zero-indexing, where `-1` indices stand for non-existing entries in the DNNs. For instance, the first four columns in the DNN prediction correspond to the four energy groups of the NGamma cross section. For the N2N reaction, on the contrary, only the first energy group contains nonzero values, so the `indices` under N2N is written to be `[4, -1, -1, -1]`, meaning that the fifth column in the DNN prediction corresponds to the first energy group of N2N reaction.
- Scattering matrix adopts a CSR representation, as illustrated by the `profile` entry.
- `reaction_scaling` gives information of the mean and standard deviation of the output variables, which will be used inside Griffin for normalization and inverse normalization of the output.

**Listing 1.** Example ISOXML file for  $^{235}\text{U}$ .

```
<ISOXML>
<Multigroup_Cross_Section_Libraries Name="U235_Example" NGroup="4" Description="Tabulation for
216 multiphysics grid points">
  <Multigroup_Cross_Section_Library ID="1" Ver="1.0" Generator="INL" TimeCreated="Fri Aug 16
12:00:00 2024" Description="Only U235">
    <Tabulation>burnup tmod tfuel</Tabulation>
    <burnup>0 39.6 79.2 118.8 158.4 198</burnup>
    <tmod>300 600 900 1200 1500 1800</tmod>
```



```

<tfuel>300 600 900 1200 1500 1800</tfuel>
<ReferenceGridIndex>1 1 1</ReferenceGridIndex>
<AllReactions>Scattering EnergyDeposition nuFission Fission kappaFission FissionSpectrum
NGamma N2N N3N N4N Removal Total Absorption</AllReactions>
<Table gridIndex="1 1 1">
  <Isotope Name="U235" I="6">
    <NGamma>0.1348724 6.630614 27.09995 44.41323</NGamma>
    <N2N>0.004449997 0 0 0</N2N>
    <N3N>2.545488e-06 0 0 0</N3N>
    <N4N>2.426214e-10 0 0 0</N4N>
    <kappaFission>3.911437e-11 3.993285e-10 1.076662e-09 7.880718e-09</kappaFission>
    <EnergyDeposition>3.911437e-11 3.993285e-10 1.076662e-09 7.880718e-09</EnergyDeposition>
    <nuFission>3.260207 31.01972 82.93536 619.8332</nuFission>
    <Fission>1.265526 12.74118 34.03849 254.3897</Fission>
    <FissionSpectrum>0.9675659 0.03243403 2.512241e-08 5.008456e-10</FissionSpectrum>
    <Scattering>
      4.245824 0 0 0
      0.2976323 11.13988 0 0
      1.735178e-07 0.007466631 11.25937 0.003390048
      1.081672e-10 0 0.06319343 14.11967
    </Scattering>
    <Removal>1.693575785 19.37926063 61.20163343 298.80632</Removal>
    <Total>5.939399785 30.51914063 72.46100343 312.92599</Total>
    <Absorption>1.404850943 19.371794 61.13844 298.80293</Absorption>
  </Isotope>
</Table>
<Table gridIndex="1 1 2">
  <Isotope Name="U235" I="6">
    <NGamma>0.134873 6.599858 27.22064 44.11464</NGamma>
    <N2N>0.004450038 0 0 0</N2N>
    <N3N>2.54551e-06 0 0 0</N3N>
    <N4N>2.426236e-10 0 0 0</N4N>
    <kappaFission>3.911456e-11 3.983343e-10 1.081802e-09 7.819203e-09</kappaFission>
    <EnergyDeposition>3.911456e-11 3.983343e-10 1.081802e-09 7.819203e-09</EnergyDeposition>
    <nuFission>3.260222 30.94362 83.33202 614.991</nuFission>
    <Fission>1.265532 12.70994 34.20128 252.4023</Fission>
    <FissionSpectrum>0.9675659 0.03243403 2.512218e-08 5.008107e-10</FissionSpectrum>
    <Scattering>
      4.245842 0 0 0
      0.2976335 11.13651 0 0
      1.735186e-07 0.007374389 11.24133 0.006258393
      1.081676e-10 0 0.0728002 14.13653
    </Scattering>
    <Removal>1.693583544 19.31717239 61.4947202 296.5231984</Removal>
    <Total>5.939425544 30.45368239 72.7360502 310.6597284</Total>
    <Absorption>1.404857584 19.309798 61.42192 296.51694</Absorption>
  </Isotope>
</Table>
...
<Table gridIndex="6 6 6">
  <Isotope Name="U235" I="6">
    <NGamma>0.1337681 6.715218 27.31218 30.55866</NGamma>
    <N2N>0.00517628 0 0 0</N2N>
    <N3N>4.090586e-06 0 0 0</N3N>
    <N4N>4.03411e-10 0 0 0</N4N>
    <kappaFission>3.910355e-11 4.04484e-10 1.099266e-09 5.096293e-09</kappaFission>
    <EnergyDeposition>3.910355e-11 4.04484e-10 1.099266e-09 5.096293e-09</EnergyDeposition>
    <nuFission>3.264013 31.42039 84.70612 400.6805</nuFission>
    <Fission>1.265212 12.9057 34.76524 164.4458</Fission>
  </Isotope>
</Table>

```

```

<FissionSpectrum>0.9675659 0.03243408 2.512447e-08 5.011621e-10</FissionSpectrum>
<Scattering>
  4.231961 0 0 0
  0.2960817 11.14545 0 0
  1.725118e-07 0.007406764 11.19673 0.008011362
  1.069803e-10 0 0.1027081 14.03032
</Scattering>
<Removal>1.68987751 19.62832476 62.1801281 195.0124714</Removal>
<Total>5.92183851 30.77377476 73.3768581 209.0427914</Total>
<Absorption>1.404160471 19.620918 62.07742 195.00446</Absorption>
</Isotope>
</Table>
</Multigroup_Cross_Section_Library>
</Multigroup_Cross_Section_Libraries>
</ISOXML>

```

---

**Listing 2.** Example JSON file for  $^{235}\text{U}$ .

```

[
  {
    "name": "U235",
    "material_id": 0,
    "model_path": "torch_models/U235.pt",
    "nGroup": 4,
    "variables": ["burnup", "tmod", "tfuel"],
    "variable_scaling": {
      "mean": [98.99493061600697, 866.6086333145579, 1433.3043166572788],
      "std": [59.03096630153866, 417.9405925331413, 417.9996080001863]
    },
    "NGamma": { "indices": [0, 1, 2, 3] },
    "N2N": { "indices": [4, -1, -1, -1] },
    "N3N": { "indices": [5, -1, -1, -1] },
    "N4N": { "indices": [6, -1, -1, -1] },
    "kappaFission": { "indices": [7, 8, 9, 10] },
    "Fission": { "indices": [11, 12, 13, 14] },
    "FissionSpectrum": { "indices": [15, 16, 17, 18] },
    "nuFission": { "indices": [19, 20, 21, 22] },
    "reactions": ["NGamma", "N2N", "N3N", "N4N", "kappaFission", "Fission", "FissionSpectrum",
    "nuFission", "Scattering"],
    "Scattering": {
      "L": 0,
      "profile": [[[0, 0], [0, 1], [0, 3], [0, 3]]],
      "indices": [23, 24, 25, 26, 27, 28, 29, 30, -1, 31, 32]
    },
    "reaction_scaling": {
      "mean": [0.1343186449556557, 6.657511361827539, 27.438999392836298, 39.48566207059758,
      0.004810791451530544, 3.307428176421732e-06, 3.21868822081571e-10, 3.910908451809105e-11,
      4.015197014868145e-10, 1.097637920477751e-09, 6.802607355871269e-09, 1.265373125120078,
      12.811413439085461, 34.708057251467054, 219.5491374082646, 0.9675659264469286,
      0.03243404792930272, 2.5122854764201733e-08, 5.009136973056465e-10, 3.2621164044134363,
      31.190742755881, 84.5667817964207, 534.9425038280507, 4.2388811066956835,
      0.29685364244912693, 11.140143336987592, 1.7301584145885606e-07, 0.007336103178906755,
      11.208083316276445, 0.009686528569245225, 1.0757046965697167e-10, 0.09223674792996057,
      14.152430022218445 ],
      "std": [0.0002736573413392828, 0.04969010827935393, 0.29702087542404443, 6.156640245555157,
      0.00020055280915807995, 4.507446041063024e-07, 4.710518436986626e-11, 2.4389651766053654e-15,
      2.4974769294303065e-12, 8.112948899018952e-12, 1.2248602628238546e-09, 7.078527194170075e-05,
      0.07940806959845453, 0.25446152845930375, 39.56410920844515, 4.798074852883878e-08,

```

```

4.79782978769713e-08, 2.1255888056120825e-12, 3.259205132629881e-13, 0.00107055839344168,
0.19341698283745895, 0.6200017994803759, 96.3999411617129, 0.0033935591392578973,
0.0003726836698462067, 0.005436011001321505, 2.665972895790751e-10, 8.936010544893546e-05,
0.013656356556014798, 0.0025990335382449527, 2.885399308334092e-13, 0.009619574510864991,
0.14394773387574383
]
}
}
]

```

Figure 5 gives more details of the Griffin implementation of the Torch interface, which reuses a significant portion of the existing ISOXML and Griffin data interface system. The Torch models (TorchXS) are used instead of an ISOXML multigroup cross-section library (MultigroupLibrary) for the base cross-section data. This cross-section data is then interpolated based on the multiphysics grid points to generate a MixingTable containing the isotope-wise interpolated cross-section data. This MixingTable and the isotope-wise number densities are used to tabulate the macroscopic cross sections stored in the Mixture. This Mixture is then used by the applicable NeutronicsMaterials (NM) to provide the cross-section data for solving the neutron transport equations. Currently, the Torch models are used in their own NeutronicsMaterial; however, the functionality to support Torch model input cross-section data is expected to be extended to all NeutronicsMaterials in Griffin.

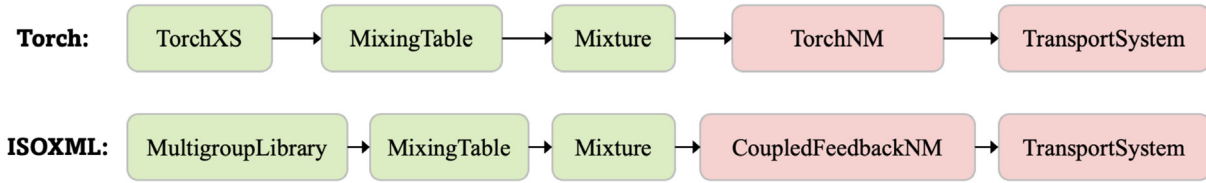


Figure 5. Griffin implementation of the Torch and ISOXML interface.

We note that currently performing the interpolation for the Torch models is significantly slower (roughly  $10\times$  slower) than performing the interpolation on an ISOXML multigroup library. Preliminary profiling has indicated that the interpolation process experiences a performance bottleneck in LibTorch itself, as a result no significant efforts to optimize the Torch model interpolation process have been made at this time. Conversely, the memory and storage space required for the Torch models is significantly smaller than that required by the ISOXML multigroup libraries for a relatively fine grid space. The entire Torch model data requires 11 MB of disk storage. By comparison, the ISOXML multigroup library covering the same grid space requires 12 GB of storage. While 12 GB of storage is not impossible to manage, a finer grid space, or the introduction of another multiphysics variable, could increase the size of the ISOXML multigroup library to exceed 1 TB, meanwhile the Torch model would be expected to still remain under 1 GB of storage space and memory requirement. However, more work is needed testing the Torch model against real-world reactor multiphysics problems to see what impact the increase in runtime and decrease in memory usage would have for practical reactor multiphysics work in Griffin.

### 3. RESULTS

#### 3.1. Downselection Of ROM Techniques

To select the appropriate ROM technique for use in cross-section generation, accuracy of the representative ROM methods is compared first. ROMs are trained to predict all energy groups of one reaction of a specific

isotope, and Figure 6 shows the true versus predicted values for the fission reaction (NFTOT) of  $^{235}\text{U}$ . Each subfigure represents such comparison for a different energy group, with  $g_1$  representing the fastest group and  $g_4$  being the slowest group. The  $R^2$  metric is evaluated on the training set and test set separately for each algorithm and is shown in the bottom of each subfigure. An accurate ROM should give predictions close to the true values (i.e., scatter points align on the diagonal line and  $R^2$  close to 1.0). It is shown in Figure 6 that:

1. PLS comes with limited expressivity and thus is unable to capture the full nonlinear relationship between the inputs and outputs, as seen by the “outliers” that deviate from the diagonal line.
2. OLS with polynomial features exhibits nice predictivity only when using a large enough polynomial order during the polynomial transformation. This work observed that a minimum polynomial order of five is required to achieve  $R^2 \geq 0.999$ .
3. Both kernel methods present great predictive accuracy, with GP outperforming SVR. Moreover, GPs provide confidence levels of the predictions, which help evaluate where the predictive accuracy awaits further improvement.
4. Tree-based algorithms are extremely powerful to capture the nonlinearity in the dataset. This work observed comparable performance between RF and XGB with the given dataset, both exhibiting great expressivity when compared with other types of algorithms.
5. DNN as a universal function approximator can be as accurate as other algorithms when tuned properly.

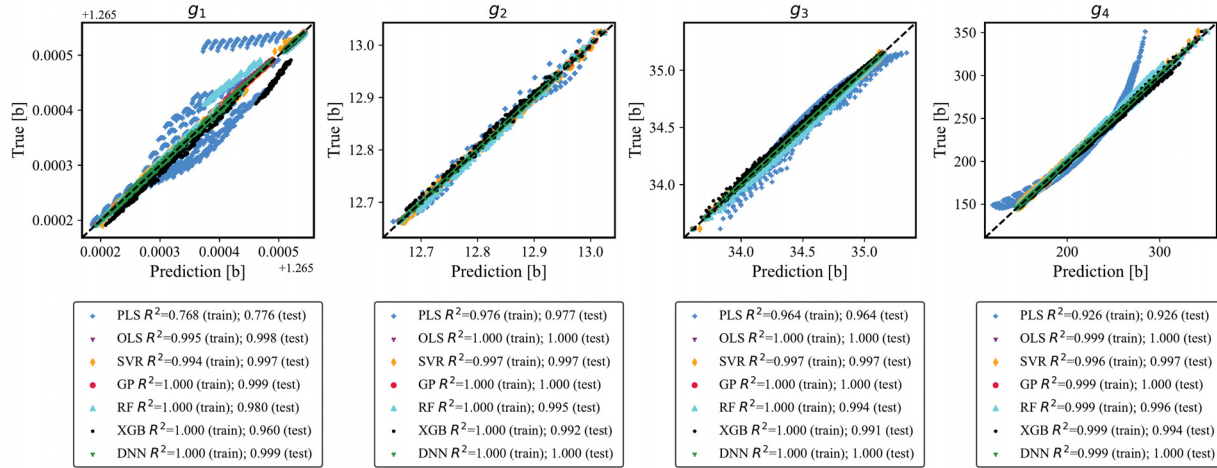


Figure 6. Comparison of the predictive accuracy of different ML algorithms for  $^{235}\text{U}$  fission reaction.

As explained in Section 2.2, selection of the ROM technique should consider many other factors than accuracy. Table 4 shows a more comprehensive performance comparison, considering the memory efficiency, training and predicting speed, and scalability of the ROM techniques, benchmarked against the multivariate interpolation method. All numbers are shown in their orders of magnitude without a loss of generality. Observations are:

1. Linear regression methods are memory efficient in general, with OLS-Poly showing superiority in both memory requirement and predictive accuracy. However, OLS-Poly exhibits poor scalability due to the employment of polynomial features, the number of which tends to grow exponentially as input dimension increases.

2. Kernel methods offer high expressiveness. However, due to the  $\mathcal{O}(N^2)$  memory requirement for storing the kernel matrix and the  $\mathcal{O}(N^3)$  computational complexity for performing matrix decomposition, scalability becomes an issue for GP for large datasets. Moreover, GPs also face challenges when dealing with high-dimensional input spaces. Nevertheless, GP-based methods remain attractive due to their ability to provide uncertainty measurements along with predictions.
3. Although showing great accuracy and scalability, tree-based algorithms are normally more memory consuming than other algorithms, with the boosting methods being more efficient than random forests. Between the two tree-based algorithms investigated in this work, XGB presents more attractiveness due to the C++ interface in the XGBoost implementation [16].
4. DNNs show superiority in memory efficiency, computational cost, and predictive accuracy. Most important of all, they exhibit extraordinary scalability to effectively accommodate a larger dataset and great flexibility when the input and output dimensionality changes. In addition, NN-based models can be easily integrated into the MOOSE framework, leveraging a recently developed LibTorch interface [7].

Table 4. Comprehensive performance comparison and downselection of ROM techniques in PyTorch.

Algorithm	Storage Size	Training Cost (sec)	Prediction Cost (sec)	Accuracy ( $R^2$ ) (Train/Test)	Scalability	Desirability
PLS	$\mathcal{O}(10^2)$ KB	$\mathcal{O}(10^{-2})$	$\mathcal{O}(10^{-4})$	0.909 / 0.911	✓	×
OLS-Poly	$\mathcal{O}(10^0)$ KB*	$\mathcal{O}(10^{-2})$	$\mathcal{O}(10^{-3})$	0.999 / 0.999	×	×
SVR	$\mathcal{O}(10^1)$ KB	$\mathcal{O}(10^{-1})$	$\mathcal{O}(10^{-4})$	0.996 / 0.997	×	×
GP	$\mathcal{O}(10^2)$ MB	$\mathcal{O}(10^2)$	$\mathcal{O}(10^{-2})$	1.000 / 1.000	×	×
RF	$\mathcal{O}(10^2)$ MB	$\mathcal{O}(10^0)$	$\mathcal{O}(10^{-1})$	1.000 / 0.991	✓	×
XGB	$\mathcal{O}(10^0)$ MB	$\mathcal{O}(10^0)$	$\mathcal{O}(10^{-3})$	1.000 / 0.984	✓	×
DNN	$\mathcal{O}(10^0)$ KB**	$\mathcal{O}(10^1 \sim 10^2)$ **	$\mathcal{O}(10^{-4})$	1.000 / 1.000	✓	✓
Interp	$\mathcal{O}(10^2)$ GB	N/A	Exponential Growth	N/A	×	×

\* Size of the OLS-poly model significantly depends on the polynomial order (polynomial order of five used in this work).

\*\* Size and training cost of DNNs depends on the detailed NN structure.

Considering all aspects, DNNs are the final choice due to their low memory requirement, fast prediction, good predictivity, and extraordinary scalability. It is important to note that the detailed NN structure strongly impacts its memory requirement and training and predicting cost. In this work, hyperparameters in the DNN model are fine-tuned through cross validation and the simplest NN structure is selected to avoid overfitting.

When comparing to the multivariate linear interpolation, DNNs show superiority in many aspects. First, DNNs carry information of the training data in the fine-tuned weights, biases, and activation functions. This eliminates the need to store all data points in their raw formats as is the case with multivariate linear interpolation, which takes in gigabytes of ISOXML files. Second, evaluation of the DNNs is fast as it only involves matrix multiplications and additions that are fast for a given NN structure with the parallel processing capabilities of modern CPUs and GPUs. Last but not the least, DNNs efficiently handle increased dimensionality and data size, allowing them to tackle increasingly complex problems across various domains. The training cost of DNNs is directly proportional to the number of epochs during hyperparameter tuning. The computational cost of DNN training is less concerning as pretrained NNs can be easily adapted with minimal training upon the availability of more data.

Overall, DNNs demonstrate high accuracy, efficiency in memory usage, and remarkable flexibility, making them an excellent choice for this work.

### 3.2. DNN As The Selected ROM For All Isotopes

In this work, a separate DNN model is trained to predict all existing reaction types for each isotope, resulting in a total number of 295 DNNs to cover all isotopes in the DRAGON5 dataset. Cross validation is adopted to select the appropriate DNN structure that ensures expressivity, and the least complex model structure (e.g., fewer neurons) is selected to avoid overfitting. The training and test error are both monitored in this work to ensure convergence of the test error during DNN training. Table 5 shows the DNN specification that has been consistently used for all isotopes.

Table 5. DNN specification for each isotope.

Specification	Value
# Hidden Layers	3
# Neurons per Layer	28
Activation Function	Gaussian Error Linear Unit (GELU)
Weight Initialization	Xavier
Optimizer	Adam
Learning Rate	5.00E-04
L2 Penalty	0
Batch Size	128
Dropout	0
Loss Function	mean squared error (MSE)
# Epochs	10,000

Taking  $^{235}\text{U}$  as an example, Figure 7 presents training errors of the DNN for all basic neutron reactions (except for the scattering matrix), and Figure 9 shows the training error for the scattering matrix. In Figure 7, each subfigure plots the DNN predictions versus true values for a basic neutron reaction. In the case of  $^{235}\text{U}$ , reactions being predicted are [NG, N2N, N3N, N4N, H-FACTOR, NFTOT, CHI, NUSIGF]. Different color codes are used for different energy groups.  $R^2$  and mean absolute percentage error (MAPE) evaluation metrics are calculated for all training data and annotated for each reaction. As mentioned in Section 2.1, the DNNs are trained only to predict nonzero entries. Therefore, in threshold reactions like N2N, N3N and N4N, only the first energy group is being predicted for  $^{235}\text{U}$ , as shown by the blue markers in the second, third, and forth columns in the first row. In Figure 9, each subfigure compares the predicted versus true values for a nonzero entry in the scattering matrix for  $^{235}\text{U}$ , along with the  $R^2$ , MAPE, RMSE, and MAE metrics. For  $^{235}\text{U}$ , there is an upscattering entry  $g_{43}$  that is three orders of magnitude lower than the self-scattering terms, and one downscattering entry  $g_{24}$  remains zero for all states of *burnup*, *tmod*, and *tfuel*. As shown by Figure 7 and Figure 9, the training error is consistently low for all reactions of  $^{235}\text{U}$ , indicating proper expressivity of the trained DNN models.

The predictive behavior of the trained DNNs is then evaluated on a separate test set for all reactions of  $^{235}\text{U}$ , as shown in Figure 8 and Figure 10. The predictive error in general is larger on the test set, with the MAPE below 0.02% for most reactions and approximately 0.04% at most. Performance evaluation on the test set ensures that the selected DNN structure is appropriate and does not overfit to the training data.

Extending this ROM construction to all isotopes, a separate DNN is trained with the selected model structure as detailed in Table 5. Note that a denser grid of DRAGON5 samples that consist of 19,529 is used as the training set for this purpose. Figure 11 summarizes the relative training error (defined as the average over all available reactions) for the 42 fissionable isotopes. For each fissionable isotope, distribution of the relative errors on all the 19,529 data points is depicted by a boxplot. The bottom and upper edge of the box represent the 25th and 75th percentile of the relative errors of DNN predictions with respect to the true data. The center red line represents the median of the data. The height of the box thus represents the Interquartile



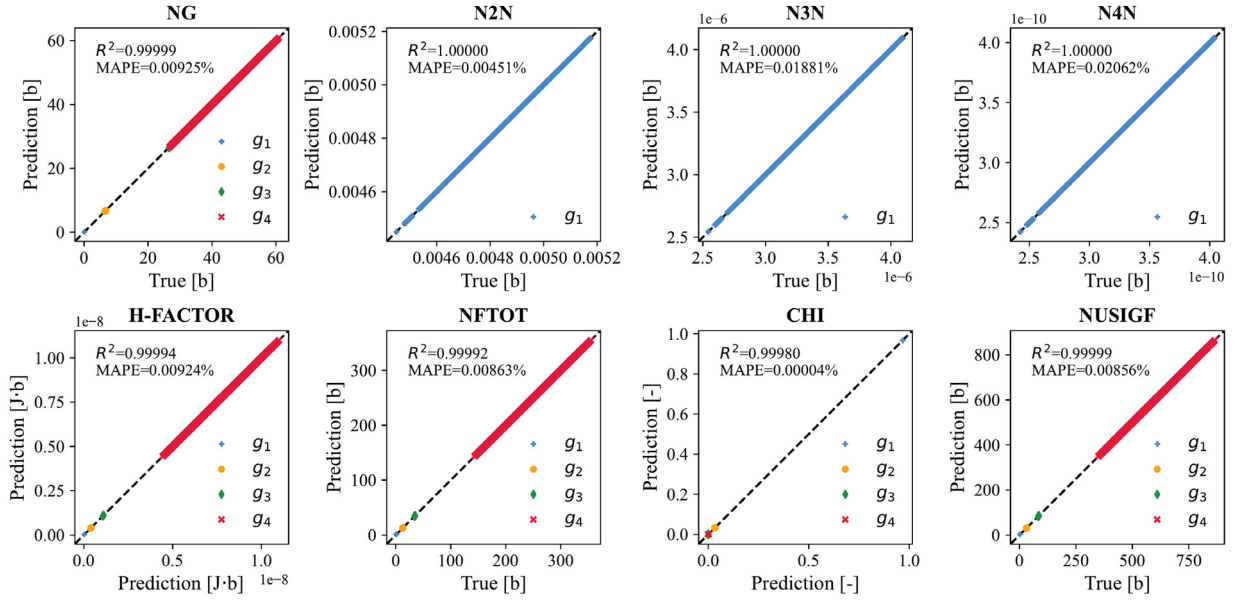


Figure 7. Prediction of the  $^{235}\text{U}$  fundamental neutron reactions (except for the scattering matrix) on the training set. Each subfigure represents a different reaction. Predicted versus true values are shown for all nonzero energy groups, along with the  $R^2$  and MAPE metrics.

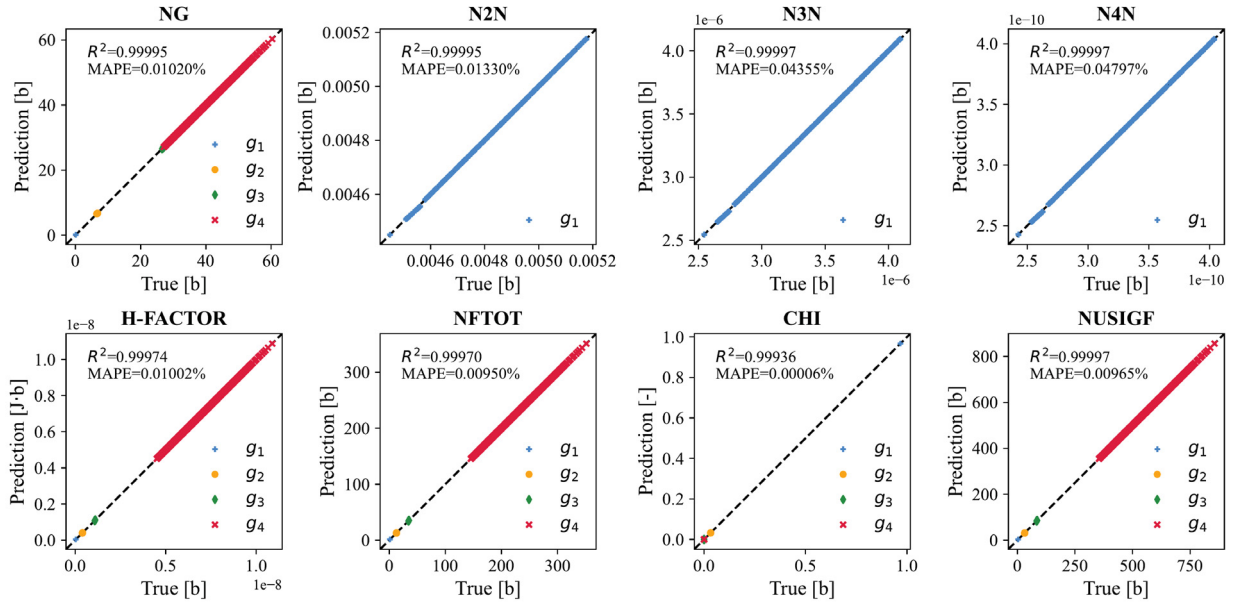


Figure 8. Prediction of the  $^{235}\text{U}$  fundamental neutron reactions (except for the scattering matrix) on the test set. Each subfigure represents a different reaction. Predicted versus true values are shown for all nonzero energy groups, along with the  $R^2$  and MAPE metrics.

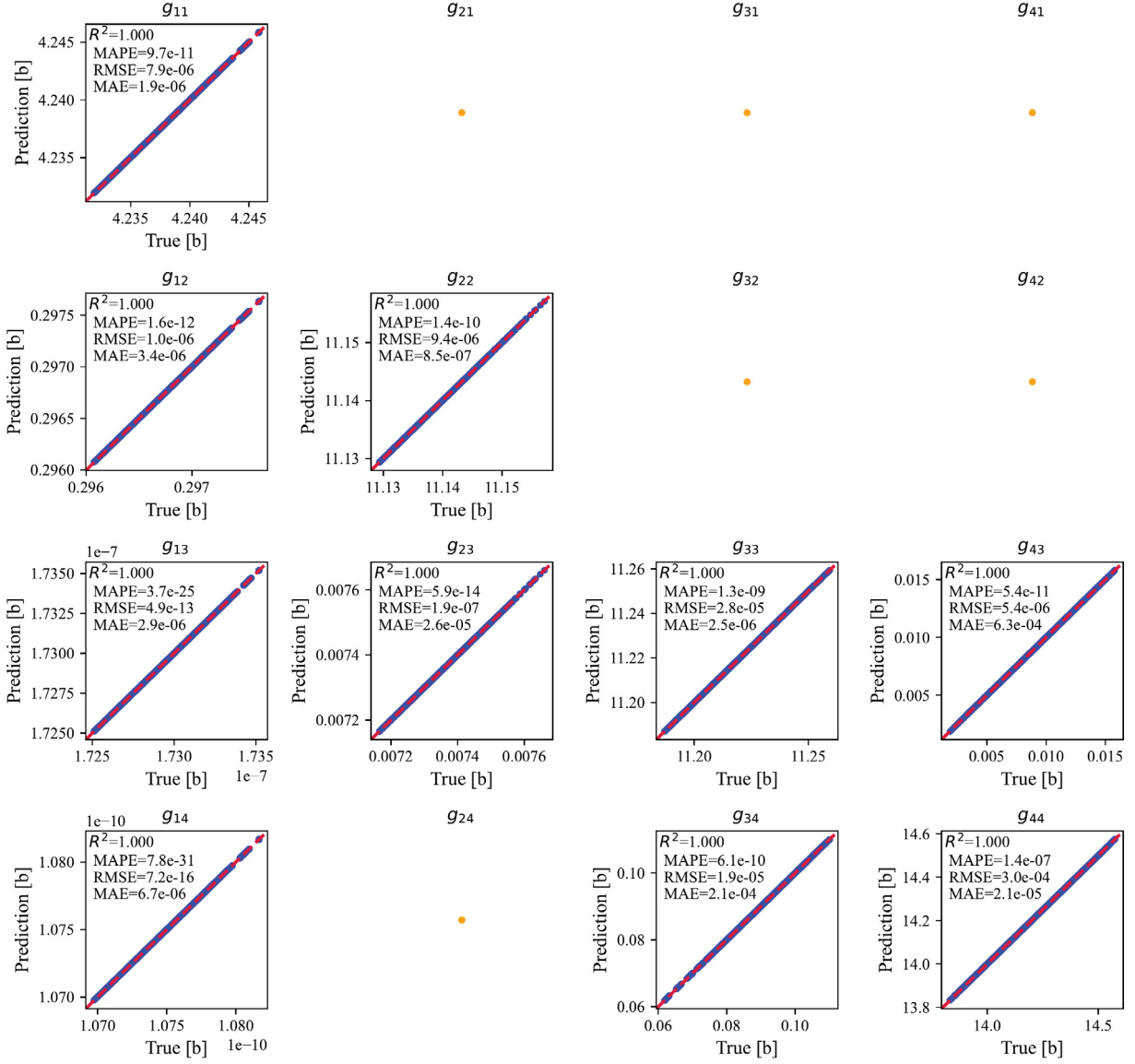


Figure 9. Prediction of the  $^{235}\text{U}$  scattering matrix on the training set. Predicted versus true values are shown for the nonzero entries in the scattering matrix, along with evaluation metrics, including  $R^2$ , MAPE, RMSE, and MAE.



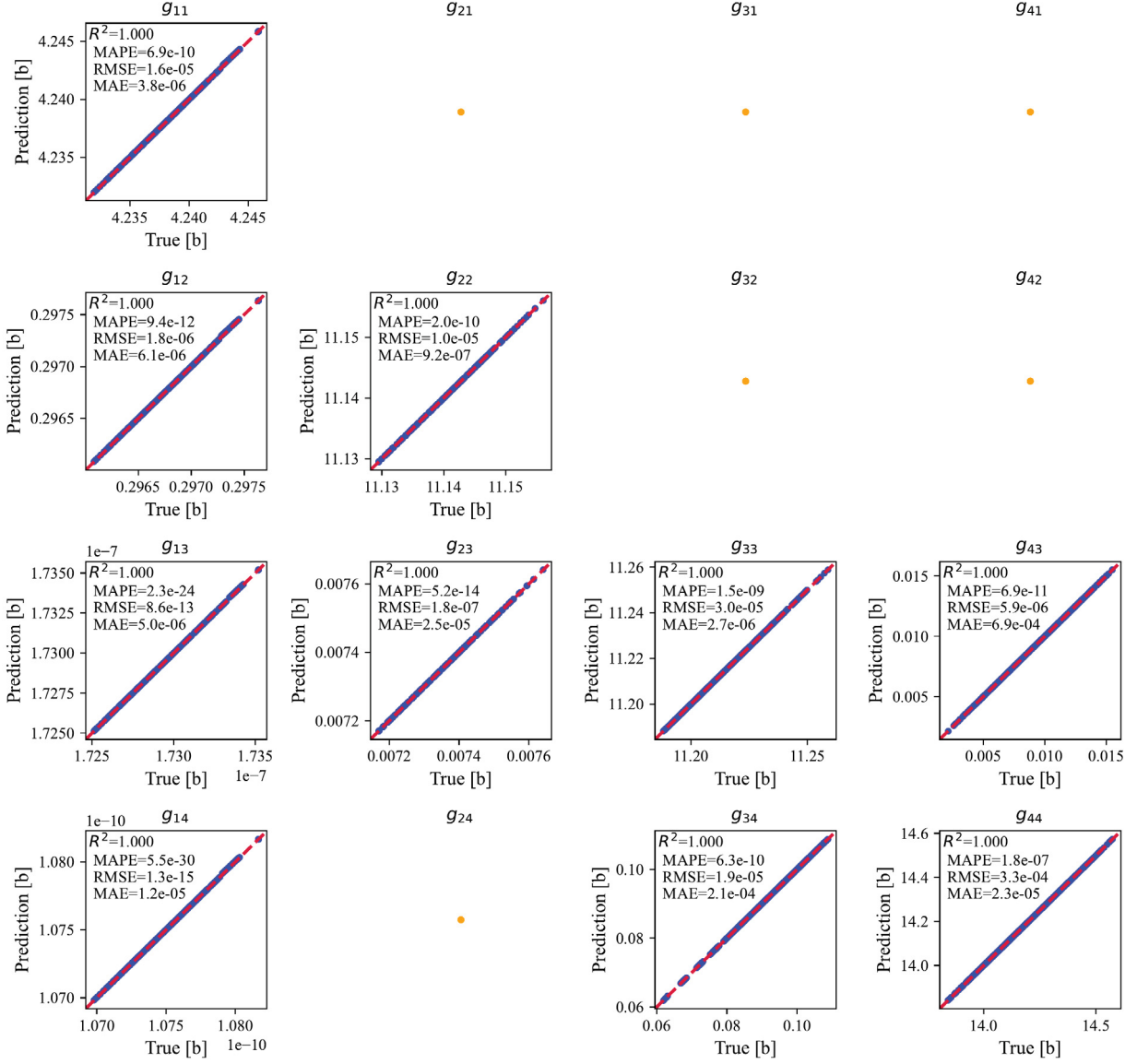


Figure 10. Prediction of the  $^{235}\text{U}$  scattering matrix on the test set. Predicted versus true values are shown for the nonzero entries in the scattering matrix, along with evaluation metrics, including  $R^2$ , MAPE, RMSE, and MAE.

Range (IQR), showing where the central 50% of the data lies. The whiskers extend from the box edges to  $1.5 \times$  the IQR below/above the 25th/75th percentile, respectively, and outliers that fall outside of the range of whiskers are denoted by orange circles. It is shown that the training error for all fissionable isotopes is primarily below  $10^{-3}$ , with the median error below  $10^{-4}$  and the maximum error approaching  $10^{-2}$  only for a few isotopes, such as  $^{242}\text{Pu}$ .

The same analysis is repeated for a total number of 253 nonfissionable isotopes in the dataset, as shown in Figure 16 in Appendix A. Again, the relative training error is calculated as the average across all available reactions for each isotope, and the distribution of the training errors across all states is summarized by boxplots. The nonfissionable isotopes do not go through fission reactions (i.e., none of NFTOT, NUSIGF, or CHI exists). Therefore, the number of neutron reactions thus the output dimensionality of the DNN is usually less than that for fissionable isotopes. As shown in Figure 16, for all nonfissionable isotopes, the 75th percentile of the training error is below  $10^{-4}$ , with outliers of certain nonfissionable isotopes reaching about  $10^{-3}$  at the maximum.

The performance of the trained DNN is then compared against multivariate linear interpolation on a separate test set that is independent of the training set. This separate test set contains a grid of state variables, with the tabulation points for each state variable spanning the full physical parameter range with six uniform samples. Figure 12 shows the absolute relative error between the prediction using DNN and multivariate linear interpolation for all reactions of  $^{235}\text{U}$  via violin plots. For each reaction, the shape of the red violin denotes a smoothed density estimate of the relative error for all possible states, and the width of the violin at any given height indicates the relative frequency of the relative error at that value. The central black dot marks the mean relative error across all states. The predictive error is larger for the thermal energy group of NG, H-FACTOR, and NUSIGF reactions; the fast energy group of N2N, N3N, and N4N; and the upscattering term of the scattering matrix (SCATRD-34), as denoted by the wider spread of the violin plots. Nevertheless, the mean absolute relative errors are effectively less than 0.06% for all reactions, and the maximum error is about 0.17% specifically for the upscattering term.

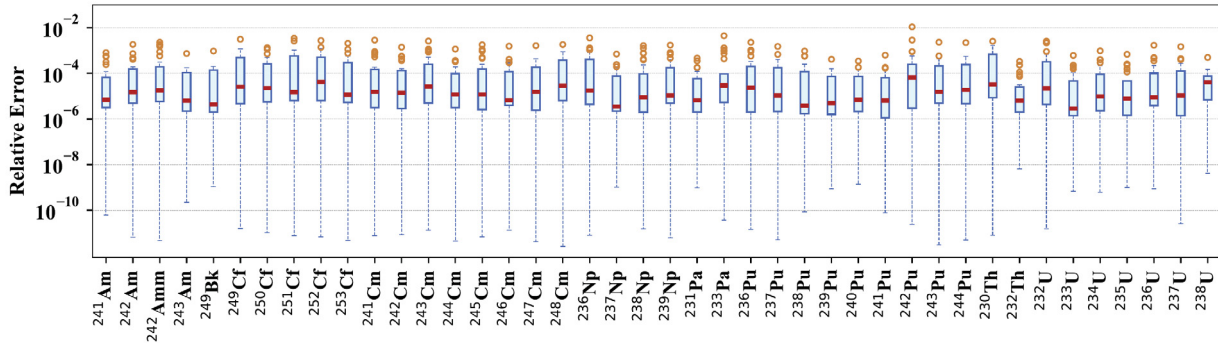


Figure 11. Relative training error of DNNs for fissionable isotopes. For each isotope, the relative error is calculated as the mean relative error across all available reactions. Red lines represent data median. Blue boxes stand for the central 50% of data. Orange circles denote outliers falling out of the 25th/75th percentile.

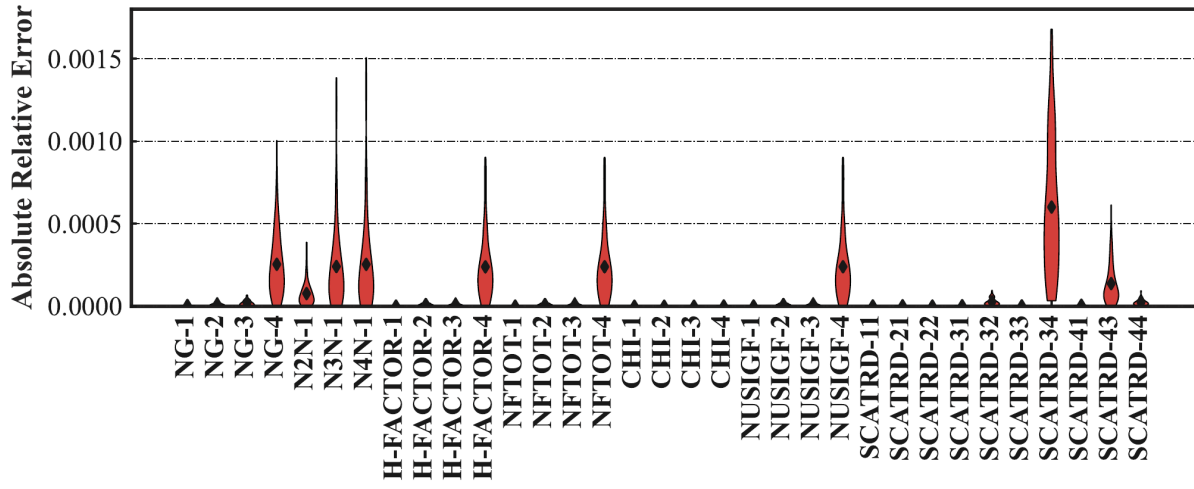


Figure 12. Comparison between DNN and multivariate linear interpolation on a uniform test grid for all reactions of  $^{235}\text{U}$ . The central black dot marks the mean relative error.

### 3.3. Griffin Testing

In order to test the DNN-predicted cross sections, DNN ROMs are loaded into Griffin through the interface as described in Section 2.3. As a preliminary test, an infinite homogeneous (0D) domain test case is performed in Griffin using the DFEM-Discrete Ordinate (SN) solver. The LibTorch model is compared against the ISOXML cross-section data that the LibTorch model was trained on. Rather than having Griffin perform linear interpolation on the ISOXML grid space, only grid points explicitly defined in the ISOXML cross-section data library were used for the calculation comparisons. This means the reference solution is not influenced by the interpolation method implemented in Griffin. For performance reasons, the ISOXML data consisted of a restricted grid space and was tested using six equidistant points across the *burnup*, *tmod*, and *tfuel* space with the assumption that *tmod* always be less than or equal to *tfuel*. This results in a total of 126 grid points tested.

The first test case simulates a homogeneous region consisting of  $^{235}\text{U}$ ,  $^{238}\text{U}$ , and graphite, as these isotopes are expected to generate the most significant contribution to the reactivity for a Beginning of Life (BOL) Pebble Bed Reactor (PBR) fuel pebble. Table 6 presents the number densities used to represent a BOL PBR where the pebbles have been homogenized with the coolant. Note that Griffin requires atomic number densities to be specified, so the exact values used in the Griffin input are provided here for reproducibility purposes.

Table 6. Isotope densities used for Griffin 0D testing.

Isotope	Density (atoms/b-cm)	Density (g/cc)
$^{235}\text{U}$	1.50E-05	0.00585
$^{238}\text{U}$	8.07E-05	0.0319
Graphite	5.19E-02	1.03

We then compared the results of the 0D test cases using the ISOXML and Torch data for all 126 grid points. When comparing the isotope-wise cross-section values for specific reactions, the errors are on the order of 0.1% for the most part. A summary of the maximum overprediction (OP), maximum underprediction (UP), mean relative difference (RD), and mean absolute RD (i.e., the average value of the sum of the absolute value of the relative differences) for several quantities of interest are shown in Table 7. The reactivity difference between the neural network prediction and the reference ISOXML data is shown in Figure 13 for various burnup values. Blue bars stand for positive differences, and red ones for negative errors. The DNN is subject to largest predictive error at zero burnup due to the cutoff in training data, as there is no way for burnups to go below zero. This obstacle can be surpassed by simply adding a data point in the training set very close to 0. Since the maximum reactivity difference is 16.2 per cent mille (pcm), it is worth pointing out that the in-core temperature predictions are subject to uncertainties in PBRs. In order to compare the reactivity difference brought in by the ROM technique with that resulted by the temperature uncertainty, we perturbed *tmod* and *tfuel* by  $\pm 50$  K using the reference ISOXML cross-section data. The resulting reaction deviation as a result of the temperature perturbation is 302 pcm, which is  $20\times$  the reactivity error brought in by the ROM technique. Therefore, accuracy of the DNN ROM trained in this work is considered acceptable, but must be taken into account explicitly during uncertainty propagation studies.

It is noted that the thermal upscattering from energy group 4 to group 3 experiences the largest deviations compared to all other cross-section values. The maximum deviations for the thermal upscattering across the grid space for each isotope are 0.265% for  $^{235}\text{U}$ , 0.0636% for  $^{238}\text{U}$ , and 2.06% for graphite. This indicates that certain cross-section quantities are more challenging for the DNN to model and further investigation of these challenges need be addressed as part of the future work. Additional figures plotting quantities of interest besides reactivity are shown in Figures 17, 18, and 19–22 in Appendix B.1 for macroscopic absorption rate,

fission rate, and neutron fluxes.

Table 7. Summary of differences between the Torch model and the ISOXML model for the  $^{235}\text{U}$ ,  $^{238}\text{U}$ , and graphite. All quantities are in units of pcm.

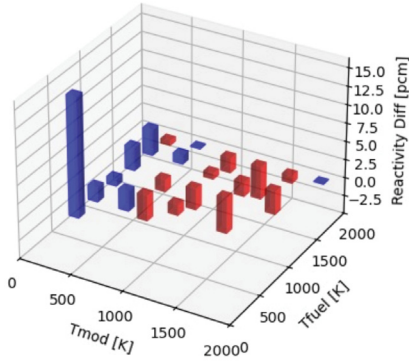
Quantity	Maximum OP	Maximum UP	Mean RD	Mean Absolute RD
Reactivity	16.3	-6.35	0.578	2.29
Fission Rate	26.5	-9.42	1.04	3.48
Absorption Rate	0.338	-0.160	0.0982	0.122
Flux G1	0.566	-0.661	-0.109	0.195
Flux G2	16.8	-2.38	1.94	2.33
Flux G3	16.2	-4.74	0.377	2.54
Flux G4	108	-58.1	-7.29	26.3

The second test case simulates an infinite homogeneous region consisting of 279 isotopes with number densities representative of an Middle of Life (MOL) fuel pebble from a PBR. These number densities are shown in Table 9 in Appendix B.2. The differences in reactivity calculated for the 279 isotope infinite homogeneous system is shown in Figure 14 and the differences in the isothermal temperature coefficient of reactivity (ITC) are shown in Figure 15. The maximum observed reactivity difference is +22.6 pcm, larger than the three-nuclide case, but not a dramatic increase. The average absolute reactivity difference across all grid points is 5.43 pcm. Additional comparisons are shown in Figures 23, 24, 25, 26, and 27–30 for the macroscopic absorption, fission reaction rates, fuel temperature coefficient of reactivity (FTC), moderator temperature coefficient of reactivity (MTC), and fluxes in each energy group in Appendix B.2, respectively. These figures highlight that the differences in fission rate are much larger than the differences in absorption rate and are driving the reactivity differences.

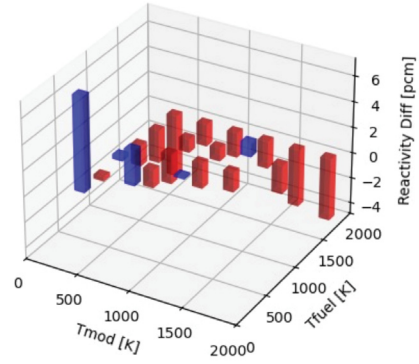
Predictive differences between using the Torch model and the ISOXML file is summarized in Table 8 for the 279-nuclide infinite homogeneous case, showing the maximum OP, maximum UP, mean RD, and mean absolute RD. As shown in Table 8, no quantity ever exceeds 50 pcm of difference and the average differences are typically on the order of several pcm; the main exception being the most thermal flux group, which is to be expected as the most thermal flux group will be the most sensitive to changes in temperatures.

Table 8. Summary of differences between the Torch model and the ISOXML model.

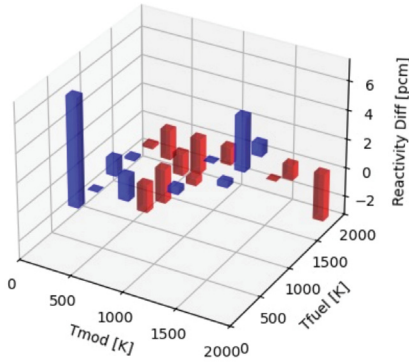
Quantity	Maximum OP	Maximum UP	Mean RD	Mean Absolute RD
Reactivity	22.6 pcm	-20.0 pcm	1.91 pcm	5.43 pcm
Fission Rate	30.0 pcm	-18.3 pcm	3.17 pcm	6.77 pcm
Absorption Rate	0.232 pcm	-0.296 pcm	0.0245 pcm	0.0630 pcm
Flux G1	0.580 pcm	-0.579 pcm	-0.0526 pcm	0.153 pcm
Flux G2	10.6 pcm	-3.89 pcm	0.500 pcm	1.69 pcm
Flux G3	10.1 pcm	-5.18 pcm	0.0507 pcm	2.12 pcm
Flux G4	37.1 pcm	-46.4 pcm	-10.1 pcm	12.2 pcm
ITC	$0.205 \frac{\text{pcm}}{\text{K}}$	$-0.170 \frac{\text{pcm}}{\text{K}}$	$-6.28 \times 10^{-4} \frac{\text{pcm}}{\text{K}}$	$0.0337 \frac{\text{pcm}}{\text{K}}$
MTC	$0.126 \frac{\text{pcm}}{\text{K}}$	$-0.171 \frac{\text{pcm}}{\text{K}}$	$-0.00457 \frac{\text{pcm}}{\text{K}}$	$0.0317 \frac{\text{pcm}}{\text{K}}$
FTC	$0.0952 \frac{\text{pcm}}{\text{K}}$	$-0.0536 \frac{\text{pcm}}{\text{K}}$	$0.00493 \frac{\text{pcm}}{\text{K}}$	$0.0187 \frac{\text{pcm}}{\text{K}}$



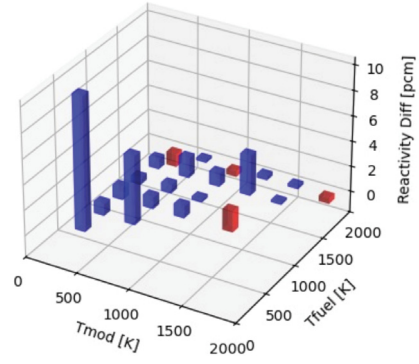
(a) Burnup=0 GWd/tHM



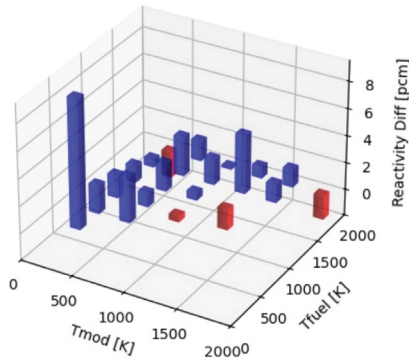
(b) Burnup=39.6 GWd/tHM



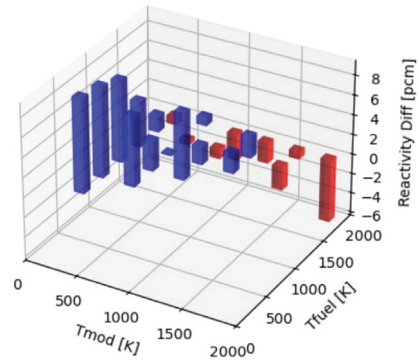
(c) Burnup=79.2 GWd/tHM



(d) Burnup=118.8 GWd/tHM



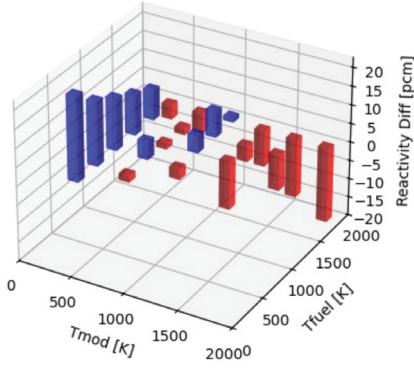
(e) Burnup=158.4 GWd/tHM



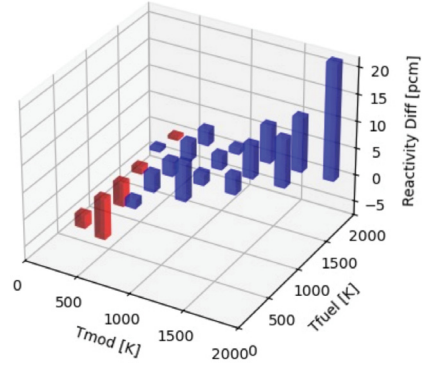
(f) Burnup=198.0 GWd/tHM

Figure 13. Simulated differences in reactivity between ISOXML data and DNN for a homogeneous region consisting  $^{235}\text{U}$ ,  $^{238}\text{U}$ , and graphite at the burnup of (a) 0 GWd/tHM, (b) 39.6 GWd/tHM, (c) 79.2 GWd/tHM, (d) 118.8 GWd/tHM, (e) 158.4 GWd/tHM, and (f) 198.0 GWd/tHM. Blue bars stand for positive differences, and red ones for negative errors.

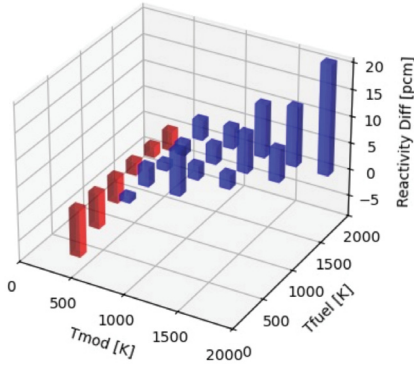




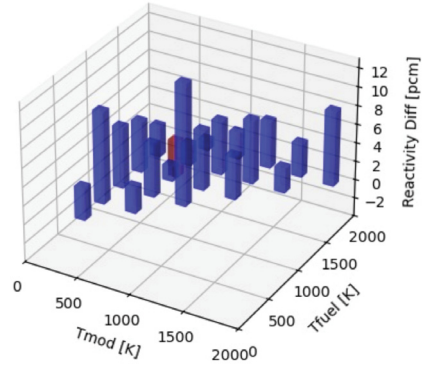
(a) Burnup=0 GWd/tHM



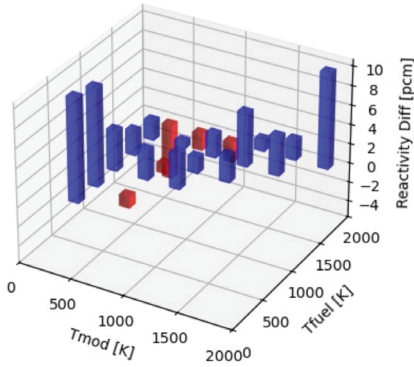
(b) Burnup=39.6 GWd/tHM



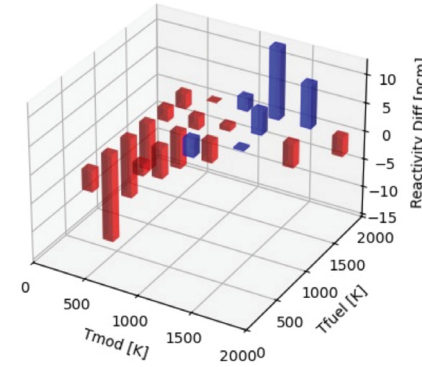
(c) Burnup=79.2 GWd/tHM



(d) Burnup=118.8 GWd/tHM

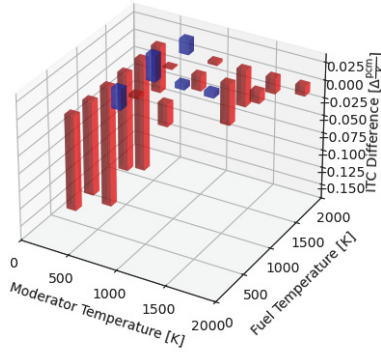


(e) Burnup=158.4 GWd/tHM

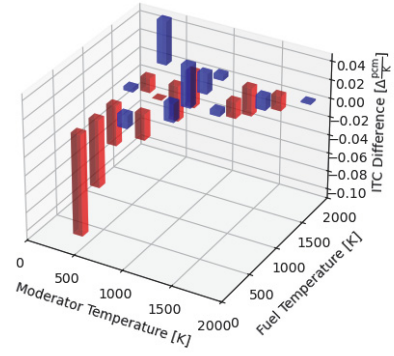


(f) Burnup=198.0 GWd/tHM

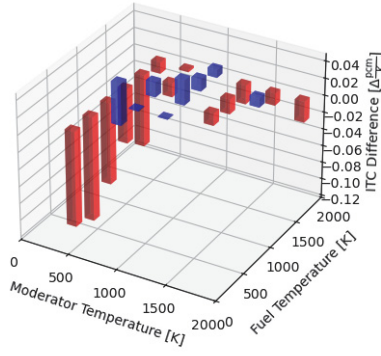
Figure 14. Simulated differences in reactivity between ISOXML data and DNN for a homogeneous region consisting of 279 isotopes with number densities representative of a MOL fuel pebble in a PBR at the burnup of (a) 0 GWd/tHM, (b) 39.6 GWd/tHM, (c) 79.2 GWd/tHM, (d) 118.8 GWd/tHM, (e) 158.4 GWd/tHM, and (f) 198.0 GWd/tHM. Blue bars stand for positive differences, and red ones for negative errors.



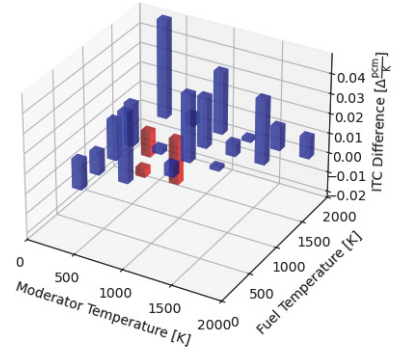
(a) Burnup=0 GWd/tHM



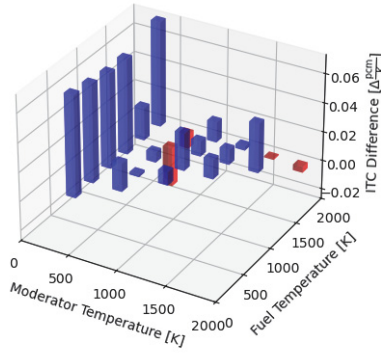
(b) Burnup=39.6 GWd/tHM



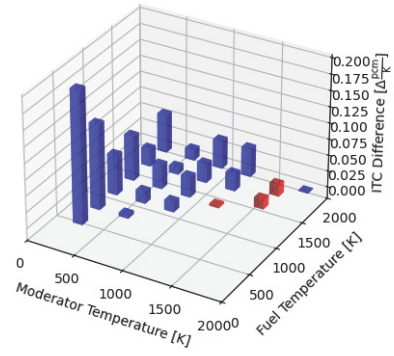
(c) Burnup=79.2 GWd/tHM



(d) Burnup=118.8 GWd/tHM



(e) Burnup=158.4 GWd/tHM



(f) Burnup=198.0 GWd/tHM

Figure 15. Simulated differences in the ITC between ISOXML data and DNN for a homogeneous region consisting of 279 isotopes with number densities representative of a MOL fuel pebble in a PBR at the burnup of (a) 0 GWd/tHM, (b) 39.6 GWd/tHM, (c) 79.2 GWd/tHM, (d) 118.8 GWd/tHM, (e) 158.4 GWd/tHM, and (f) 198.0 GWd/tHM. Blue bars stand for positive differences, and red ones for negative errors.



## 4. CONCLUSION

This work has presented a systematic study of downselection and application of ROM techniques to support the microscopic multigroup cross-section evaluation in Griffin. Based on the pregenerated PBR cross-section data, NN-based algorithms stand out as the best technique with high memory efficiency, excellent predictive accuracy, great scalability, ease of integration into the MOOSE framework, and superior flexibility during the retraining process. Preliminary Griffin testing has revealed some early promise of using DNN as the ROM, as it introduces small errors in the predicted reactivity. Although the DNN can lead to stochastic biases in temperature reactivity coefficients, we have shown that the bias is roughly  $\pm 1\%$  in an infinite homogeneous domain and should decrease in more realistic models. Furthermore, this effect is small compared to the error associated with the inherent temperature uncertainties for PBRs. A separate DNN has been trained for each isotope for all fundamental neutron reactions, and the composite neutron reactions are derived from the DNN predictions within Griffin. The DNN models have been prepared for all isotopes this year for future depletion simulations.

Listed below are the key findings in this work regarding the DNN training:

1. It is essential to train the DNN to only predict fundamental reactions for calculating the derived reactions. This helps avoid error accumulation when predicting derived neutron reactions.
2. The training set of the DNN should only include physical data points, for example, state variable that satisfy  $t_{fuel} \geq t_{mod}$ , for faster training and improved DNN performance.
3. The DNN should be trained to only predict nonzero energy groups to avoid high output dimensionality, as discussed in this report. An alternative way to handle the mixed-zero data is to train a classifier to predict whether data for a certain energy group should be zero (returning 0 if seeing all-zero data and 1.0 vice versa), then multiply the classifier prediction with the DNN prediction, as has been showcased in reference [19].
4. The DNN model tends to be more accurate within the training data range, but its predictive accuracy slightly diminishes near the parameter boundaries. This indicates a need for finer training data near the boundaries for enhanced performance near the parameter boundaries, especially for the zero burnup.
5. Prediction of the upscattering entries in the scattering matrix, which is correlated to the total cross section and removal cross section, awaits further improvement. Efforts should be devoted into improving the prediction of the upscattering entries in the future to achieve improved performance in general.

Overall, this work showcased DNN as a promising ROM technique that can be used to generate isotopic multigroup neutron cross sections in support of Griffin simulations. This DNN model effectively replaces gigabyte-sized ISOXML cross-section files with Torch models that are only tens of kilobytes per isotope. With improvements in memory efficiency by orders of magnitude, the ROM technique enables the consideration of more state variables during cross-section generation—something difficult to achieve with the ISOXML method due to memory constraints. Eventually, it will accelerate and improve the fidelity of the PBR simulation in Griffin.

## 5. FUTURE WORK

This year's work downselected DNN as a promising ROM technique and demonstrated the capability of DNNs on pregenerated cross-section data. The long-term goal is to integrate ROMs with the online cross-section generation capability in Griffin [20] to enable on-the-fly generation of cross sections and concurrent update of the ROMs. Future work will primarily focus on two key aspects:

1. This work showcased a preliminary Griffin testing on a 0D homogeneous problem. Parallel to this work, systematic Griffin testings on more complex problems are being conducted as well. Moreover, current work focused on solving the steady-state neutron transport equations, and future work will include depletion simulations to further demonstrate the feasibility and effectiveness of this ROM technique. This work showed the feasibility of DNNs as a ROM technique on a simple dataset of only four energy groups and three state variables. Future work will focus on practical problems that involve a much larger number of state variables and energy groups, in which case dimensionality reduction techniques will be incorporated.
2. Integrating ROMs with the Griffin online cross-section generation requires embedding the ROM training and cross-section generation into an active learning scheme [21]. This goal necessitates implementing an active learning framework in Griffin, as well as the investigation into ROM methods with uncertainty predictions. Multiple DNN-based algorithms show promise in providing uncertainty estimations while maintaining superior memory efficiency and predictive accuracy and thus will be considered in the future work.

## 6. REFERENCES

- [1] Qin, S., Zhang, Q., Zhang, J., Liang, L., Zhao, Q., Wu, H., and Cao, L. (2020) Application of deep neural network for generating resonance self-shielded cross-section. *Annals of Nuclear Energy*, **149**, 107785.
- [2] Ravichandran, M., Gentry, C., and Bucci, M., Investigation into the use of machine learning assisted prediction of nodal parameters for reduced order neutronic simulation models. Technical report, Oak Ridge National Laboratory (ORNL), Oak Ridge, TN (United States) (2021).
- [3] Nicolas Martin, Zachary Prince, V. L. and Tano-Retamales, M. (2023) Deep Learning for Multigroup Cross-Section Representation in Two-Step Core Calculations. *Nuclear Science and Engineering*, **197**(7), 1406–1435.
- [4] Chan, Y. M. and Dufek, J. (2024) A deep-learning representation of multi-group cross sections in lattice calculations. *Annals of Nuclear Energy*, **195**, 110123.
- [5] Paszke, A., Gross, S., Chintala, S., Chanan, G., Yang, E., DeVito, Z., Lin, Z., Desmaison, A., Antiga, L., and Lerer, A. (2017) Automatic Differentiation in PyTorch. In *Proceedings of the 31st International Conference on Neural Information Processing Systems (NIPS 2017)* Red Hook, NY, USA: Curran Associates, Inc. pp. 8024–8035.
- [6] Paszke, A., Gross, S., Massa, F., Lerer, A., Bradbury, J., Chanan, G., Killeen, T., Lin, Z., Gimelshein, N., Antiga, L., et al. (2019) PyTorch: An imperative style, high-performance deep learning library. *Advances in neural information processing systems*, **32**.
- [7] German, P. and Yushu, D. (2023) Enabling scientific machine learning in MOOSE using LibTorch. *SoftwareX*, **23**, 101489.
- [8] Hébert, A. (2013) DRAGON5: designing computational schemes dedicated to fission nuclear reactors for space. *Proceedings of Nuclear and Emerging Technologies for Space*, **25**.
- [9] Massimo, L. (2013) Physics of high-temperature reactors, Elsevier, Amsterdam, Netherlands.
- [10] Saad, Y. (2003) Iterative methods for sparse linear systems, SIAM, Philadelphia, PA.

- [11] Abdi, H. (2010) Partial least squares regression and projection on latent structure regression (PLS Regression). *Wiley interdisciplinary reviews: computational statistics*, **2**(1), 97–106.
- [12] Hofmann, T., Schölkopf, B., and Smola, A. J. (2008) Kernel methods in machine learning. *The Annals of Statistics*,.
- [13] Awad, M., Khanna, R., Awad, M., and Khanna, R. (2015) Support vector regression. *Efficient learning machines: Theories, concepts, and applications for engineers and system designers*, pp. 67–80.
- [14] Theodoridis, S. and Koutroumbas, K. (2006) Pattern recognition, Elsevier, Amsterdam, Netherlands.
- [15] Geurts, P., Ernst, D., and Wehenkel, L. (2006) Extremely randomized trees. *Machine learning*, **63**, 3–42.
- [16] Chen, T. and Guestrin, C. (2016) Xgboost: A scalable tree boosting system. In *Proceedings of the 22nd acm sigkdd international conference on knowledge discovery and data mining* pp. 785–794.
- [17] Goodfellow, I. (2016) Deep Learning, MIT Press, Cambridge, Massachusetts, USA.
- [18] Press, W. H. (2007) Numerical recipes 3rd edition: The art of scientific computing, Cambridge university press, Cambridge, United Kingdom.
- [19] Che, Y., Balestra, P., Ortensi, J., Calvin, O., Wang, Y., Park, H., and Deshmukh, A. (2024) Reduced-Order Modeling of Multigroup Neutron Cross Sections for High-Temperature Gas-cooled Reactors. In *International Topical Meeting on High Temperature Reactor Technology*.
- [20] Park, H., Jung, Y. S., Lee, C., Wang, Y., and Ortensi, J. (2024) Initial Assessment of Online Cross Section Generation Capability of Griffin for Gas-Cooled Pebble-bed Reactor. In *Int. Conf. on Physics of Reactors*.
- [21] Settles, B. (2009) Active learning literature survey, University of Wisconsin-Madison Department of Computer Sciences, Madison, Wisconsin.



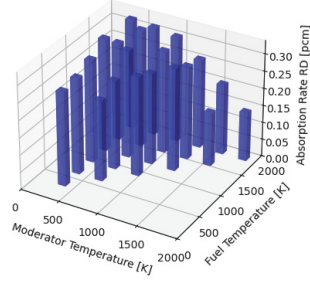
## Appendix B

### Complementary Results for Griffin Testing

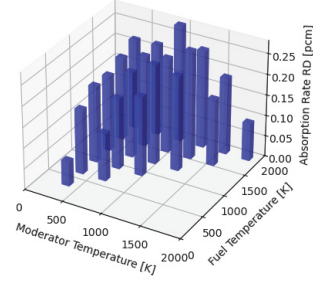
This appendix provides Griffin testing results that complement those in Section 3.3.

#### B.1. Infinite Homogeneous Region Of Three Isotopes

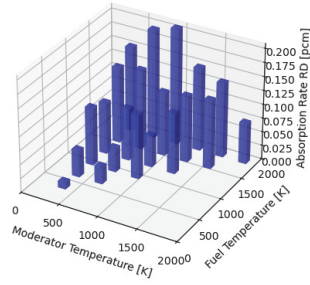
A detailed and systematic comparison between using the ISOXML data and the DNN ROM in Griffin is presented in this section for the infinite homogeneous region consisting of the three isotopes as shown in Table 6. The simulated differences for a representative PBR fuel pebble are shown at different burnups for the macroscopic absorption rate (Figure 17), the macroscopic fission rate (Figure 18), and the neutron fluxes for the first energy group (Figure 19), second energy group (Figure 20), third energy group (Figure 21), and fourth energy group (Figure 22).



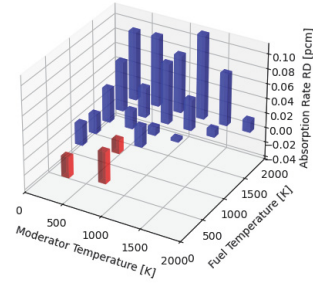
(a) Burnup=0 GWd/tHM



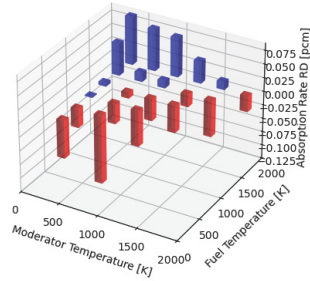
(b) Burnup=39.6 GWd/tHM



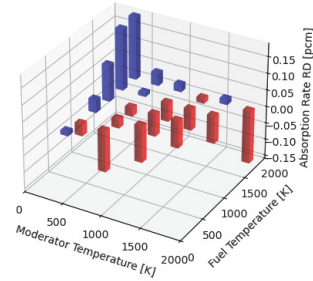
(c) Burnup=79.2 GWd/tHM



(d) Burnup=118.8 GWd/tHM



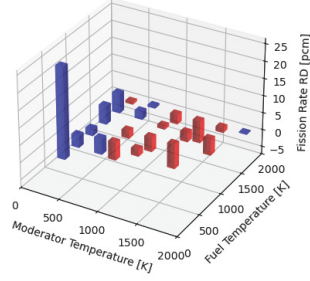
(e) Burnup=158.4 GWd/tHM



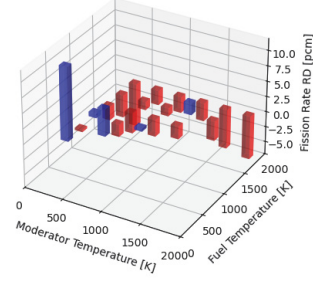
(f) Burnup=198.0 GWd/tHM

Figure 17. Simulated differences in the macroscopic absorption rate between ISOXML data and DNN for a homogeneous region consisting of  $^{235}\text{U}$ ,  $^{238}\text{U}$ , and graphite with number densities representative of a BOL PBR fuel pebble at the burnup of (a) 0 GWd/tHM, (b) 39.6 GWd/tHM, (c) 79.2 GWd/tHM, (d) 118.8 GWd/tHM, (e) 158.4 GWd/tHM, and (f) 198.0 GWd/tHM.

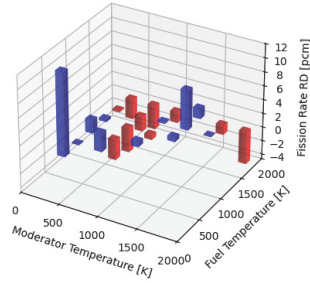




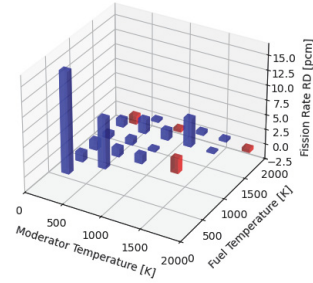
(a) Burnup=0 GWd/tHM



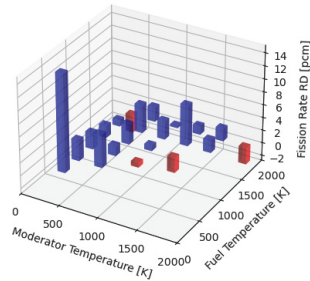
(b) Burnup=39.6 GWd/tHM



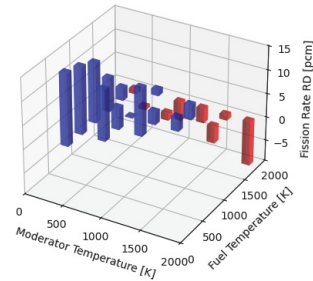
(c) Burnup=79.2 GWd/tHM



(d) Burnup=118.8 GWd/tHM

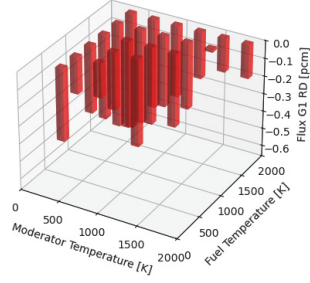


(e) Burnup=158.4 GWd/tHM

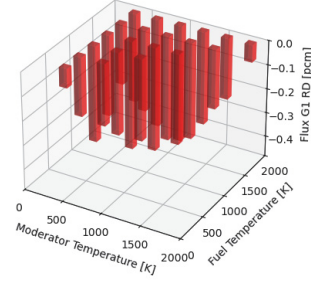


(f) Burnup=198.0 GWd/tHM

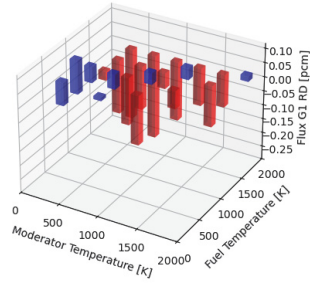
Figure 18. Simulated differences in the macroscopic fission rate between ISOXML data and DNN for a homogeneous region consisting of  $^{235}\text{U}$ ,  $^{238}\text{U}$ , and graphite with number densities representative of a BOL PBR fuel pebble at the burnup of (a) 0 GWd/tHM, (b) 39.6 GWd/tHM, (c) 79.2 GWd/tHM, (d) 118.8 GWd/tHM, (e) 158.4 GWd/tHM, and (f) 198.0 GWd/tHM.



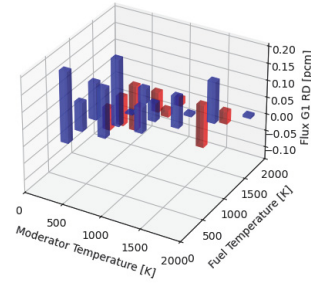
(a) Burnup=0 GWd/tHM



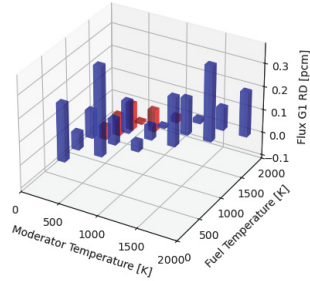
(b) Burnup=39.6 GWd/tHM



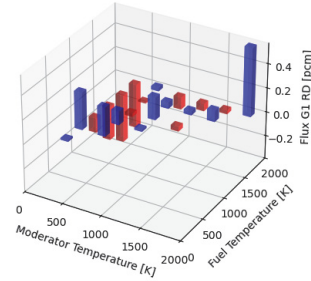
(c) Burnup=79.2 GWd/tHM



(d) Burnup=118.8 GWd/tHM



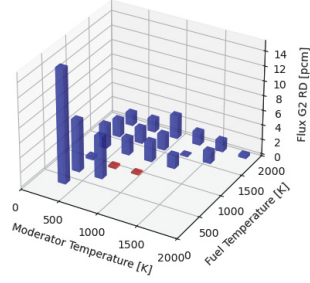
(e) Burnup=158.4 GWd/tHM



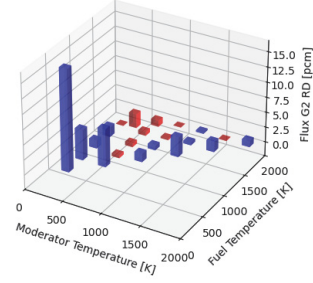
(f) Burnup=198.0 GWd/tHM

Figure 19. Simulated differences in the neutron flux in Energy Group 1 between ISOXML data and DNN for a homogeneous region consisting of  $^{235}\text{U}$ ,  $^{238}\text{U}$ , and graphite with number densities representative of a BOL PBR fuel pebble at the burnup of (a) 0 GWd/tHM, (b) 39.6 GWd/tHM, (c) 79.2 GWd/tHM, (d) 118.8 GWd/tHM, (e) 158.4 GWd/tHM, and (f) 198.0 GWd/tHM.

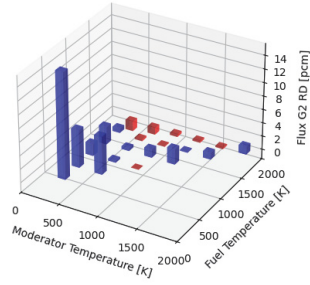




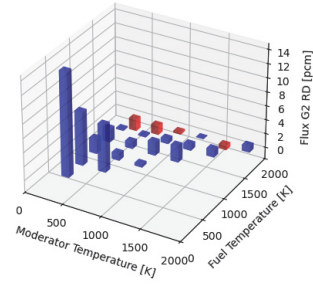
(a) Burnup=0 GWd/tHM



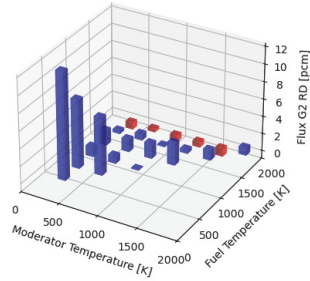
(b) Burnup=39.6 GWd/tHM



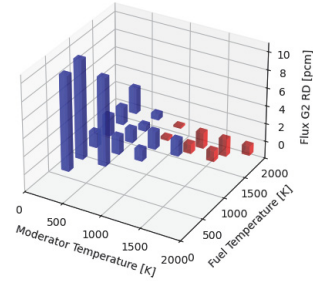
(c) Burnup=79.2 GWd/tHM



(d) Burnup=118.8 GWd/tHM

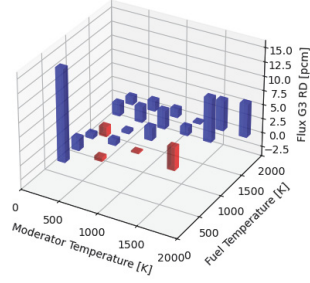


(e) Burnup=158.4 GWd/tHM

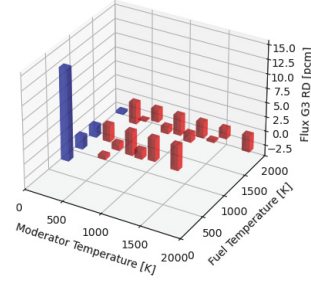


(f) Burnup=198.0 GWd/tHM

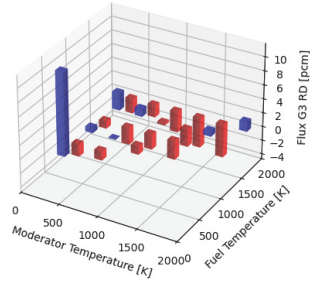
Figure 20. Simulated differences in the neutron flux in Energy Group 2 between ISOXML data and DNN for a homogeneous region consisting of  $^{235}\text{U}$ ,  $^{238}\text{U}$ , and graphite with number densities representative of a BOL PBR fuel pebble at the burnup of (a) 0 GWd/tHM, (b) 39.6 GWd/tHM, (c) 79.2 GWd/tHM, (d) 118.8 GWd/tHM, (e) 158.4 GWd/tHM, and (f) 198.0 GWd/tHM.



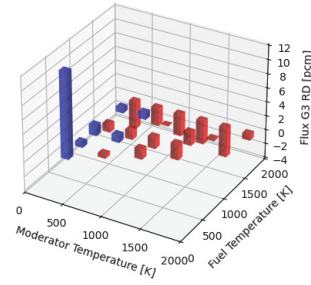
(a) Burnup=0 GWd/tHM



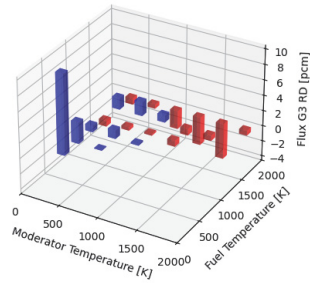
(b) Burnup=39.6 GWd/tHM



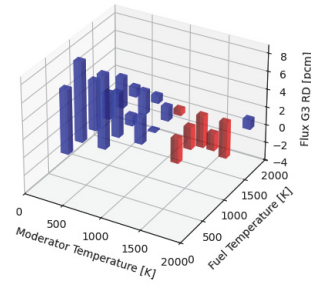
(c) Burnup=79.2 GWd/tHM



(d) Burnup=118.8 GWd/tHM

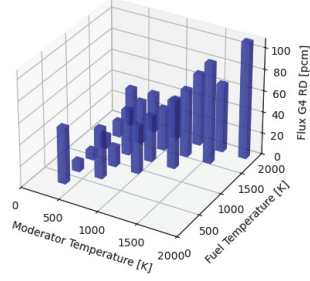


(e) Burnup=158.4 GWd/tHM

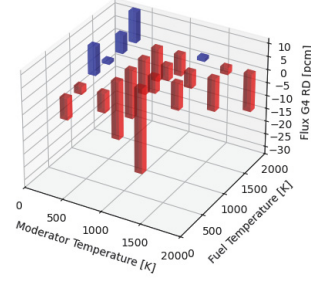


(f) Burnup=198.0 GWd/tHM

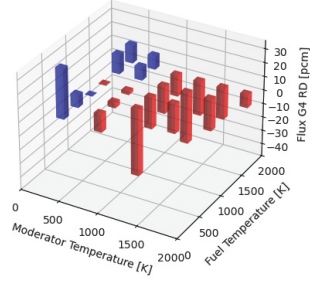
Figure 21. Simulated differences in the neutron flux in Energy Group 3 between ISOXML data and DNN for a homogeneous region consisting of  $^{235}\text{U}$ ,  $^{238}\text{U}$ , and graphite with number densities representative of a BOL PBR fuel pebble at the burnup of (a) 0 GWd/tHM, (b) 39.6 GWd/tHM, (c) 79.2 GWd/tHM, (d) 118.8 GWd/tHM, (e) 158.4 GWd/tHM, and (f) 198.0 GWd/tHM.



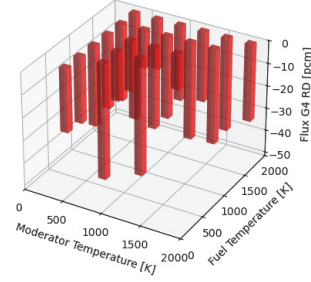
(a) Burnup=0 GWd/tHM



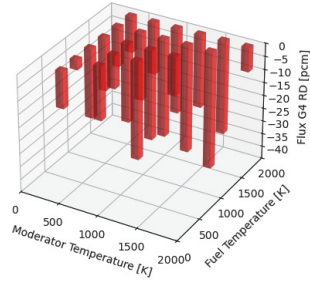
(b) Burnup=39.6 GWd/tHM



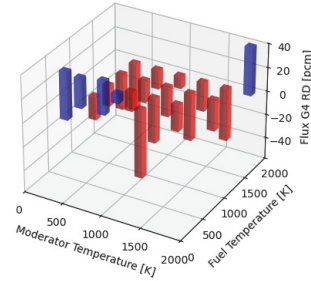
(c) Burnup=79.2 GWd/tHM



(d) Burnup=118.8 GWd/tHM



(e) Burnup=158.4 GWd/tHM



(f) Burnup=198.0 GWd/tHM

Figure 22. Simulated differences in the neutron flux in Energy Group 4 between ISOXML data and DNN for a homogeneous region consisting of  $^{235}\text{U}$ ,  $^{238}\text{U}$ , and graphite with number densities representative of a BOL PBR fuel pebble at the burnup of (a) 0 GWd/tHM, (b) 39.6 GWd/tHM, (c) 79.2 GWd/tHM, (d) 118.8 GWd/tHM, (e) 158.4 GWd/tHM, and (f) 198.0 GWd/tHM.

## B.2. Infinite Homogeneous Region Of 279 Isotopes

Similar to the three-isotope problem, this section presents a detailed comparison between using the ISOXML data and the DNN ROM in Griffin for the infinite homogenous problem with 279 isotopes. Table 9 gives the exact isotopic number densities that have been used for this test case. The simulated differences for a representative PBR fuel pebble are shown at different burnups for the macroscopic absorption rate (Figure 23), the macroscopic fission rate (Figure 24), and the neutron fluxes for the first energy group (Figure 27), second energy group (Figure 28), third energy group (Figure 29), and forth energy group (Figure 30).

Table 9. MOL PBR fuel pebble nuclide number densities.

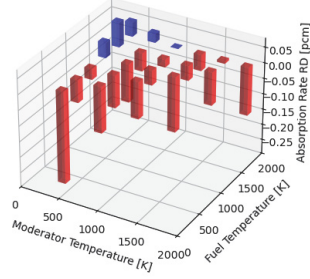
Nuclide	Number Density [ $\frac{\text{atoms}}{\text{b}\cdot\text{cm}}$ ]	Nuclide	Number Density [ $\frac{\text{atoms}}{\text{b}\cdot\text{cm}}$ ]
<sup>107</sup> Ag	$1.37941077 \times 10^{-14}$	<sup>109</sup> Ag	$4.15433732 \times 10^{-8}$
<sup>111</sup> Ag	$3.26768557 \times 10^{-10}$	<sup>27</sup> Al	$6.16239785 \times 10^{-12}$
<sup>241</sup> Am	$1.14031877 \times 10^{-8}$	<sup>242</sup> Am	$4.45230137 \times 10^{-11}$
<sup>242m</sup> Am	$2.48029930 \times 10^{-10}$	<sup>243</sup> Am	$2.28170247 \times 10^{-8}$
<sup>75</sup> As	$1.77585960 \times 10^{-10}$	<sup>10</sup> B	$7.50707205 \times 10^{-11}$
<sup>11</sup> B	$8.96296868 \times 10^{-8}$	<sup>134</sup> Ba	$2.02304999 \times 10^{-8}$
<sup>135</sup> Ba	$6.92018387 \times 10^{-11}$	<sup>136</sup> Ba	$9.76868630 \times 10^{-9}$
<sup>137</sup> Ba	$2.53624659 \times 10^{-8}$	<sup>138</sup> Ba	$1.08880499 \times 10^{-6}$
<sup>140</sup> Ba	$2.00448245 \times 10^{-8}$	<sup>9</sup> Be	$3.09331138 \times 10^{-15}$
<sup>209</sup> Bi	$3.71472053 \times 10^{-19}$	<sup>249</sup> Bk	$9.12822344 \times 10^{-18}$
<sup>79</sup> Br	$3.76785669 \times 10^{-12}$	<sup>81</sup> Br	$3.13585602 \times 10^{-8}$
<sup>12</sup> C	$5.40011795 \times 10^{-4}$	Graphite	0.0850037783
<sup>106</sup> Cd	$1.40625010 \times 10^{-26}$	<sup>108</sup> Cd	$1.22971151 \times 10^{-14}$
<sup>110</sup> Cd	$1.11010898 \times 10^{-8}$	<sup>111</sup> Cd	$1.54185091 \times 10^{-8}$
<sup>112</sup> Cd	$7.54064988 \times 10^{-9}$	<sup>113</sup> Cd	$8.30932545 \times 10^{-11}$
<sup>114</sup> Cd	$9.31254629 \times 10^{-9}$	<sup>115m</sup> Cd	$1.68439013 \times 10^{-11}$
<sup>116</sup> Cd	$3.55282825 \times 10^{-9}$	<sup>140</sup> Ce	$9.75730472 \times 10^{-7}$
<sup>141</sup> Ce	$4.85498148 \times 10^{-8}$	<sup>142</sup> Ce	$9.27451538 \times 10^{-7}$
<sup>143</sup> Ce	$1.94289540 \times 10^{-9}$	<sup>144</sup> Ce	$3.57936756 \times 10^{-7}$
<sup>249</sup> Cf	$1.04586649 \times 10^{-18}$	<sup>250</sup> Cf	$3.77419683 \times 10^{-18}$
<sup>251</sup> Cf	$1.21235323 \times 10^{-18}$	<sup>252</sup> Cf	$9.35525039 \times 10^{-19}$
<sup>253</sup> Cf	$9.86180034 \times 10^{-22}$	<sup>35</sup> Cl	$2.00850080 \times 10^{-24}$
<sup>37</sup> Cl	$1.60922884 \times 10^{-32}$	<sup>241</sup> Cm	$1.56971815 \times 10^{-16}$
<sup>242</sup> Cm	$5.04888797 \times 10^{-9}$	<sup>243</sup> Cm	$8.14181431 \times 10^{-11}$
<sup>244</sup> Cm	$4.69026418 \times 10^{-9}$	<sup>245</sup> Cm	$1.72974191 \times 10^{-10}$
<sup>246</sup> Cm	$8.13991062 \times 10^{-12}$	<sup>247</sup> Cm	$4.61225872 \times 10^{-14}$
<sup>248</sup> Cm	$1.51258189 \times 10^{-15}$	<sup>59</sup> Co	$7.82449605 \times 10^{-29}$
<sup>52</sup> Cr	$2.80259693 \times 10^{-45}$	<sup>53</sup> Cr	$2.08793471 \times 10^{-43}$
<sup>54</sup> Cr	$6.82082028 \times 10^{-41}$	<sup>133</sup> Cs	$9.96277436 \times 10^{-7}$
<sup>134</sup> Cs	$7.94146686 \times 10^{-8}$	<sup>135</sup> Cs	$3.31862481 \times 10^{-7}$
<sup>136</sup> Cs	$3.84170945 \times 10^{-10}$	<sup>137</sup> Cs	$1.00175771 \times 10^{-6}$
<sup>63</sup> Cu	$9.12143694 \times 10^{-21}$	<sup>65</sup> Cu	$9.44985028 \times 10^{-18}$
<sup>160</sup> Dy	$5.04062556 \times 10^{-11}$	<sup>161</sup> Dy	$1.70039691 \times 10^{-10}$
<sup>162</sup> Dy	$1.07274217 \times 10^{-10}$	<sup>163</sup> Dy	$6.58105098 \times 10^{-11}$
<sup>164</sup> Dy	$1.35623041 \times 10^{-11}$	<sup>166</sup> Er	$4.45890807 \times 10^{-12}$
<sup>167</sup> Er	$1.77371667 \times 10^{-13}$	<sup>151</sup> Eu	$1.07986189 \times 10^{-11}$
<sup>152</sup> Eu	$1.79389802 \times 10^{-11}$	<sup>153</sup> Eu	$7.15871025 \times 10^{-8}$

<sup>154</sup> Eu	$1.06392051 \times 10^{-8}$	<sup>155</sup> Eu	$3.57484908 \times 10^{-9}$
<sup>156</sup> Eu	$1.99733186 \times 10^{-9}$	<sup>157</sup> Eu	$8.77448635 \times 10^{-12}$
<sup>56</sup> Fe	$2.73602893 \times 10^{-36}$	<sup>57</sup> Fe	$4.18124534 \times 10^{-34}$
<sup>58</sup> Fe	$3.64725959 \times 10^{-34}$	<sup>152</sup> Gd	$2.44868362 \times 10^{-13}$
<sup>154</sup> Gd	$6.14155171 \times 10^{-10}$	<sup>155</sup> Gd	$3.43317839 \times 10^{-11}$
<sup>156</sup> Gd	$3.12956949 \times 10^{-8}$	<sup>157</sup> Gd	$6.12873016 \times 10^{-11}$
<sup>158</sup> Gd	$7.55793650 \times 10^{-9}$	<sup>160</sup> Gd	$4.94710384 \times 10^{-10}$
<sup>72</sup> Ge	$7.60585345 \times 10^{-12}$	<sup>73</sup> Ge	$2.14905004 \times 10^{-11}$
<sup>74</sup> Ge	$6.53941901 \times 10^{-11}$	<sup>76</sup> Ge	$4.90652408 \times 10^{-10}$
<sup>4</sup> He	$1.22951627 \times 10^{-12}$	<sup>165</sup> Ho	$1.89531897 \times 10^{-11}$
<sup>127</sup> I	$3.33618750 \times 10^{-8}$	<sup>129</sup> I	$1.13424129 \times 10^{-7}$
<sup>130</sup> I	$6.32697453 \times 10^{-12}$	<sup>131</sup> I	$6.87127910 \times 10^{-9}$
<sup>135</sup> I	$4.69095929 \times 10^{-10}$	<sup>113</sup> In	$5.81889432 \times 10^{-11}$
<sup>115</sup> In	$1.56758284 \times 10^{-9}$	<sup>80</sup> Kr	$2.07082425 \times 10^{-13}$
<sup>82</sup> Kr	$4.97923980 \times 10^{-10}$	<sup>83</sup> Kr	$6.55876988 \times 10^{-8}$
<sup>84</sup> Kr	$1.39419484 \times 10^{-7}$	<sup>85</sup> Kr	$2.66552380 \times 10^{-8}$
<sup>86</sup> Kr	$2.41998833 \times 10^{-7}$	<sup>138</sup> La	$5.83540334 \times 10^{-12}$
<sup>139</sup> La	$1.01745593 \times 10^{-6}$	<sup>140</sup> La	$2.69975997 \times 10^{-9}$
<sup>6</sup> Li	$2.82443533 \times 10^{-16}$	<sup>7</sup> Li	$2.20483436 \times 10^{-8}$
<sup>24</sup> Mg	$2.46660865 \times 10^{-16}$	<sup>25</sup> Mg	$8.94055441 \times 10^{-10}$
<sup>26</sup> Mg	$9.48747261 \times 10^{-11}$	<sup>55</sup> Mn	$3.31687347 \times 10^{-42}$
<sup>100</sup> Mo	$1.04889148 \times 10^{-6}$	<sup>92</sup> Mo	$1.82175830 \times 10^{-24}$
<sup>94</sup> Mo	$6.18404633 \times 10^{-13}$	<sup>95</sup> Mo	$8.10561517 \times 10^{-7}$
<sup>96</sup> Mo	$2.57863118 \times 10^{-8}$	<sup>97</sup> Mo	$9.55252517 \times 10^{-7}$
<sup>98</sup> Mo	$9.50517688 \times 10^{-7}$	<sup>99</sup> Mo	$4.51215110 \times 10^{-9}$
<sup>14</sup> N	$3.32648338 \times 10^{-14}$	<sup>15</sup> N	$5.43265465 \times 10^{-13}$
<sup>23</sup> Na	$4.96620711 \times 10^{-18}$	<sup>93</sup> Nb	$4.89942180 \times 10^{-13}$
<sup>94</sup> Nb	$6.42878979 \times 10^{-13}$	<sup>95</sup> Nb	$5.70114871 \times 10^{-8}$
<sup>142</sup> Nd	$1.00281010 \times 10^{-8}$	<sup>143</sup> Nd	$7.05118680 \times 10^{-7}$
<sup>144</sup> Nd	$6.64159359 \times 10^{-7}$	<sup>145</sup> Nd	$5.66875940 \times 10^{-7}$
<sup>146</sup> Nd	$5.17872593 \times 10^{-7}$	<sup>147</sup> Nd	$6.29489127 \times 10^{-9}$
<sup>148</sup> Nd	$2.79713959 \times 10^{-7}$	<sup>150</sup> Nd	$1.21108428 \times 10^{-7}$
<sup>60</sup> Ni	$1.29640768 \times 10^{-27}$	<sup>61</sup> Ni	$7.06758704 \times 10^{-28}$
<sup>62</sup> Ni	$4.67611661 \times 10^{-26}$	<sup>64</sup> Ni	$2.51240343 \times 10^{-19}$
<sup>236</sup> Np	$8.43354368 \times 10^{-15}$	<sup>237</sup> Np	$1.59783127 \times 10^{-7}$
<sup>238</sup> Np	$4.58742183 \times 10^{-10}$	<sup>239</sup> Np	$3.18173718 \times 10^{-8}$
<sup>16</sup> O	$2.24033938 \times 10^{-4}$	<sup>17</sup> O	$1.31882866 \times 10^{-10}$
<sup>31</sup> P	$6.34830055 \times 10^{-9}$	<sup>231</sup> Pa	$1.51095296 \times 10^{-14}$
<sup>233</sup> Pa	$5.21704067 \times 10^{-15}$	<sup>204</sup> Pb	$2.85878985 \times 10^{-30}$
<sup>206</sup> Pb	$5.93860467 \times 10^{-21}$	<sup>207</sup> Pb	$5.02341358 \times 10^{-19}$
<sup>208</sup> Pb	$1.42241078 \times 10^{-16}$	<sup>104</sup> Pd	$1.47298081 \times 10^{-7}$
<sup>105</sup> Pd	$3.16901634 \times 10^{-7}$	<sup>106</sup> Pd	$1.30862503 \times 10^{-7}$
<sup>107</sup> Pd	$1.58498679 \times 10^{-7}$	<sup>108</sup> Pd	$1.02326439 \times 10^{-7}$
<sup>110</sup> Pd	$3.33201378 \times 10^{-8}$	<sup>147</sup> Pm	$1.71750358 \times 10^{-7}$
<sup>148</sup> Pm	$1.15328636 \times 10^{-9}$	<sup>148m</sup> Pm	$8.03694833 \times 10^{-10}$
<sup>149</sup> Pm	$9.22663168 \times 10^{-10}$	<sup>151</sup> Pm	$1.83021195 \times 10^{-10}$
<sup>141</sup> Pr	$8.71221800 \times 10^{-7}$	<sup>142</sup> Pr	$3.22931126 \times 10^{-11}$

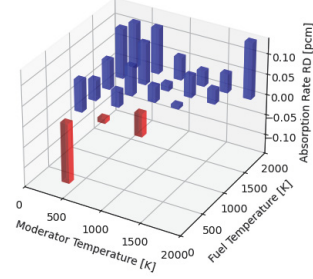
<sup>143</sup> Pr	$1.91454550 \times 10^{-8}$	<sup>236</sup> Pu	$3.16444394 \times 10^{-14}$
<sup>237</sup> Pu	$1.23973299 \times 10^{-15}$	<sup>238</sup> Pu	$4.18555963 \times 10^{-8}$
<sup>239</sup> Pu	$1.49014022 \times 10^{-6}$	<sup>240</sup> Pu	$6.69773101 \times 10^{-7}$
<sup>241</sup> Pu	$5.49470485 \times 10^{-7}$	<sup>242</sup> Pu	$2.07549405 \times 10^{-7}$
<sup>243</sup> Pu	$3.85195591 \times 10^{-11}$	<sup>244</sup> Pu	$2.36881716 \times 10^{-12}$
<sup>85</sup> Rb	$9.35714510 \times 10^{-8}$	<sup>87</sup> Rb	$3.62501652 \times 10^{-7}$
<sup>103</sup> Rh	$4.60280319 \times 10^{-7}$	<sup>105</sup> Rh	$1.10509224 \times 10^{-9}$
<sup>100</sup> Ru	$7.52812781 \times 10^{-8}$	<sup>101</sup> Ru	$8.62163745 \times 10^{-7}$
<sup>102</sup> Ru	$8.06914272 \times 10^{-7}$	<sup>103</sup> Ru	$4.93689534 \times 10^{-8}$
<sup>104</sup> Ru	$4.86745762 \times 10^{-7}$	<sup>105</sup> Ru	$1.49732782 \times 10^{-10}$
<sup>106</sup> Ru	$1.39186966 \times 10^{-7}$	<sup>99</sup> Ru	$3.46053429 \times 10^{-11}$
<sup>32</sup> S	$9.03132766 \times 10^{-13}$	<sup>33</sup> S	$2.36938726 \times 10^{-16}$
<sup>34</sup> S	$3.07816912 \times 10^{-20}$	<sup>36</sup> S	$4.04802308 \times 10^{-28}$
<sup>121</sup> Sb	$2.94546432 \times 10^{-9}$	<sup>123</sup> Sb	$3.38719719 \times 10^{-9}$
<sup>124</sup> Sb	$2.04390602 \times 10^{-11}$	<sup>125</sup> Sb	$6.41386055 \times 10^{-9}$
<sup>126</sup> Sb	$8.37638639 \times 10^{-12}$	<sup>76</sup> Se	$3.50601514 \times 10^{-12}$
<sup>77</sup> Se	$1.20156818 \times 10^{-9}$	<sup>78</sup> Se	$3.35087535 \times 10^{-9}$
<sup>79</sup> Se	$6.79278545 \times 10^{-9}$	<sup>80</sup> Se	$1.96723988 \times 10^{-8}$
<sup>82</sup> Se	$4.89610485 \times 10^{-8}$	<sup>28</sup> Si	$4.41219803 \times 10^{-4}$
<sup>29</sup> Si	$2.25176627 \times 10^{-5}$	<sup>30</sup> Si	$1.47707187 \times 10^{-5}$
<sup>147</sup> Sm	$5.34241238 \times 10^{-8}$	<sup>148</sup> Sm	$8.77088269 \times 10^{-8}$
<sup>149</sup> Sm	$1.91167771 \times 10^{-9}$	<sup>150</sup> Sm	$1.95736490 \times 10^{-7}$
<sup>151</sup> Sm	$1.09105516 \times 10^{-8}$	<sup>152</sup> Sm	$8.46350048 \times 10^{-8}$
<sup>153</sup> Sm	$6.08776640 \times 10^{-10}$	<sup>154</sup> Sm	$2.11530402 \times 10^{-8}$
<sup>112</sup> Sn	$6.09929979 \times 10^{-18}$	<sup>114</sup> Sn	$4.15004012 \times 10^{-12}$
<sup>115</sup> Sn	$1.49340595 \times 10^{-10}$	<sup>116</sup> Sn	$1.54900615 \times 10^{-9}$
<sup>117</sup> Sn	$3.24555693 \times 10^{-9}$	<sup>118</sup> Sn	$2.68431899 \times 10^{-9}$
<sup>119</sup> Sn	$2.84686297 \times 10^{-9}$	<sup>120</sup> Sn	$2.78334134 \times 10^{-9}$
<sup>122</sup> Sn	$3.61708952 \times 10^{-9}$	<sup>123</sup> Sn	$1.42101941 \times 10^{-10}$
<sup>124</sup> Sn	$6.20156149 \times 10^{-9}$	<sup>125</sup> Sn	$6.70967726 \times 10^{-11}$
<sup>126</sup> Sn	$1.42157042 \times 10^{-8}$	<sup>86</sup> Sr	$2.37717068 \times 10^{-10}$
<sup>87</sup> Sr	$1.50560760 \times 10^{-12}$	<sup>88</sup> Sr	$4.88221872 \times 10^{-7}$
<sup>89</sup> Sr	$4.80293210 \times 10^{-8}$	<sup>90</sup> Sr	$7.76795446 \times 10^{-7}$
<sup>159</sup> Tb	$1.13150533 \times 10^{-9}$	<sup>160</sup> Tb	$2.23099404 \times 10^{-11}$
<sup>99</sup> Tc	$9.30621468 \times 10^{-7}$	<sup>122</sup> Te	$1.29472530 \times 10^{-10}$
<sup>123</sup> Te	$1.03464524 \times 10^{-12}$	<sup>124</sup> Te	$8.05232200 \times 10^{-11}$
<sup>125</sup> Te	$1.74274140 \times 10^{-9}$	<sup>126</sup> Te	$5.28015465 \times 10^{-10}$
<sup>127m</sup> Te	$6.48378740 \times 10^{-10}$	<sup>128</sup> Te	$7.35224219 \times 10^{-8}$
<sup>129m</sup> Te	$1.06131426 \times 10^{-9}$	<sup>130</sup> Te	$3.19438925 \times 10^{-7}$
<sup>132</sup> Te	$3.91922228 \times 10^{-9}$	<sup>230</sup> Th	$5.28854550 \times 10^{-16}$
<sup>232</sup> Th	$9.31861129 \times 10^{-14}$	<sup>232</sup> U	$1.83608960 \times 10^{-14}$
<sup>233</sup> U	$7.75357765 \times 10^{-14}$	<sup>234</sup> U	$2.81707463 \times 10^{-10}$
<sup>235</sup> U	$9.35075059 \times 10^{-6}$	<sup>236</sup> U	$2.64114169 \times 10^{-6}$
<sup>237</sup> U	$4.47905135 \times 10^{-9}$	<sup>238</sup> U	$1.25258914 \times 10^{-4}$
<sup>128</sup> Xe	$1.24500810 \times 10^{-9}$	<sup>129</sup> Xe	$5.07279635 \times 10^{-12}$
<sup>130</sup> Xe	$3.10276227 \times 10^{-9}$	<sup>131</sup> Xe	$3.93720029 \times 10^{-7}$
<sup>132</sup> Xe	$8.50733954 \times 10^{-7}$	<sup>133</sup> Xe	$9.51829016 \times 10^{-9}$

$^{134}\text{Xe}$	$1.28946897 \times 10^{-6}$	$^{135}\text{Xe}$	$1.96039823 \times 10^{-10}$
$^{136}\text{Xe}$	$1.85827230 \times 10^{-6}$	$^{89}\text{Y}$	$6.05219100 \times 10^{-7}$
$^{90}\text{Y}$	$2.02954611 \times 10^{-10}$	$^{91}\text{Y}$	$7.12615176 \times 10^{-8}$
$^{66}\text{Zn}$	$1.82897825 \times 10^{-14}$	$^{67}\text{Zn}$	$7.14081097 \times 10^{-14}$
$^{68}\text{Zn}$	$1.63868024 \times 10^{-13}$	$^{70}\text{Zn}$	$1.23139238 \times 10^{-12}$
$^{90}\text{Zr}$	$2.19698233 \times 10^{-8}$	$^{91}\text{Zr}$	$7.44492297 \times 10^{-7}$
$^{92}\text{Zr}$	$8.66634991 \times 10^{-7}$	$^{93}\text{Zr}$	$9.31172963 \times 10^{-7}$
$^{94}\text{Zr}$	$9.75146463 \times 10^{-7}$	$^{95}\text{Zr}$	$1.01519042 \times 10^{-7}$
$^{96}\text{Zr}$	$9.79881975 \times 10^{-7}$		

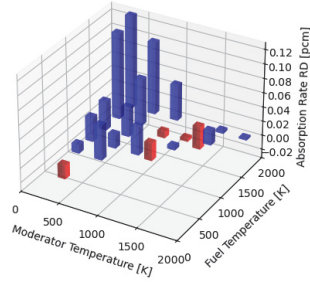




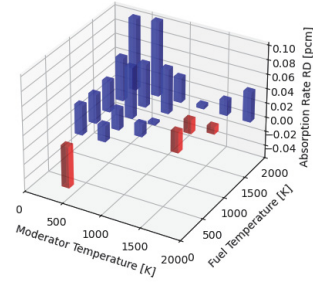
(a) Burnup=0 GWd/tHM



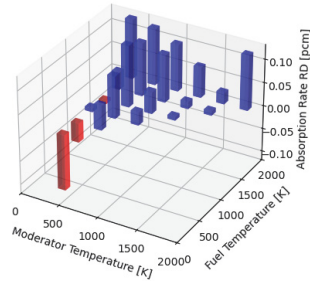
(b) Burnup=39.6 GWd/tHM



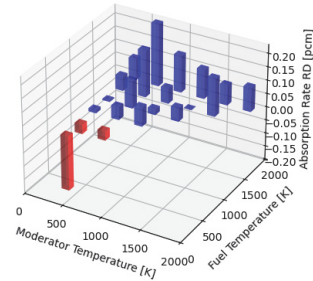
(c) Burnup=79.2 GWd/tHM



(d) Burnup=118.8 GWd/tHM



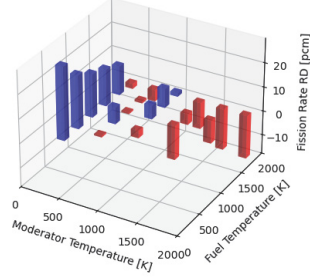
(e) Burnup=158.4 GWd/tHM



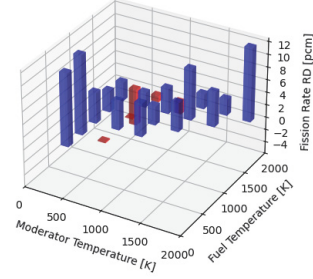
(f) Burnup=198.0 GWd/tHM

Figure 23. Simulated differences in the macroscopic absorption rate between ISOXML data and DNN for a homogeneous region consisting of 279 isotopes with number densities representative of a MOL PBR fuel pebble at the burnup of (a) 0 GWd/tHM, (b) 39.6 GWd/tHM, (c) 79.2 GWd/tHM, (d) 118.8 GWd/tHM, (e) 158.4 GWd/tHM, and (f) 198.0 GWd/tHM.

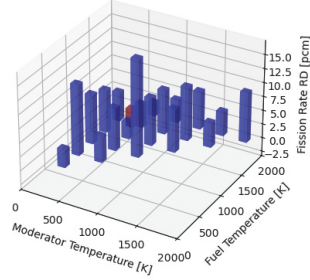




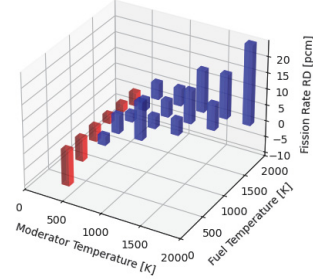
(a) Burnup=0 GWd/tHM



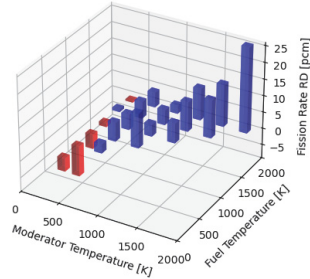
(b) Burnup=39.6 GWd/tHM



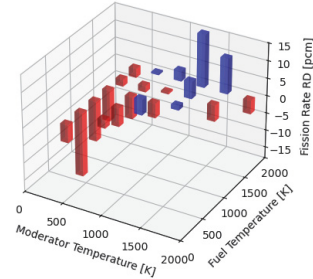
(c) Burnup=79.2 GWd/tHM



(d) Burnup=118.8 GWd/tHM

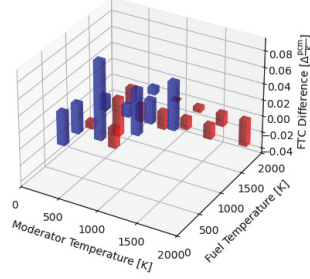


(e) Burnup=158.4 GWd/tHM

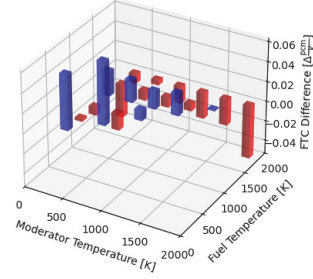


(f) Burnup=198.0 GWd/tHM

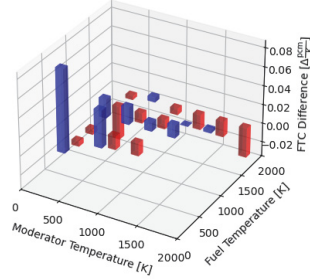
Figure 24. Simulated differences in the macroscopic fission rate between ISOXML data and DNN for a homogeneous region consisting of 279 isotopes with number densities representative of a MOL PBR fuel pebble at the burnup of (a) 0 GWd/tHM, (b) 39.6 GWd/tHM, (c) 79.2 GWd/tHM, (d) 118.8 GWd/tHM, (e) 158.4 GWd/tHM, and (f) 198.0 GWd/tHM.



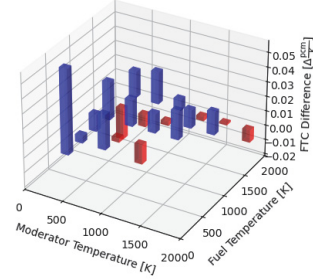
(a) Burnup=0 GWd/tHM



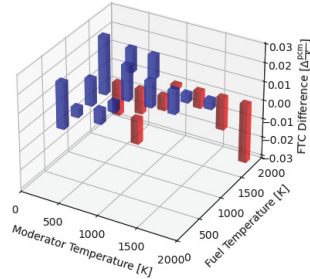
(b) Burnup=39.6 GWd/tHM



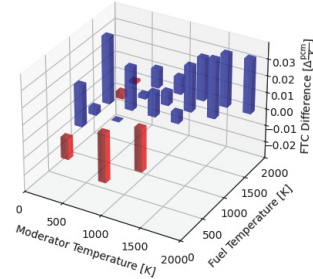
(c) Burnup=79.2 GWd/tHM



(d) Burnup=118.8 GWd/tHM

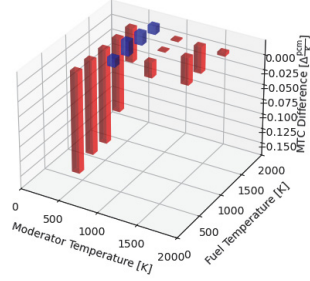


(e) Burnup=158.4 GWd/tHM

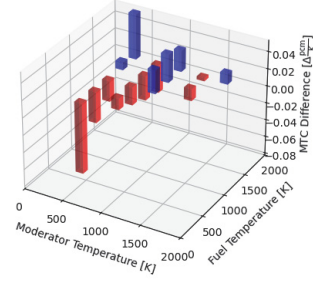


(f) Burnup=198.0 GWd/tHM

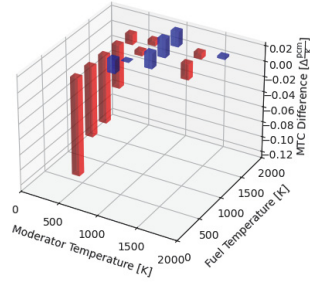
Figure 25. Simulated differences in the FTC between ISOXML data and DNN for a homogeneous region consisting of 279 isotopes with number densities representative of a MOL PBR fuel pebble at the burnup of (a) 0 GWd/tHM, (b) 39.6 GWd/tHM, (c) 79.2 GWd/tHM, (d) 118.8 GWd/tHM, (e) 158.4 GWd/tHM, and (f) 198.0 GWd/tHM.



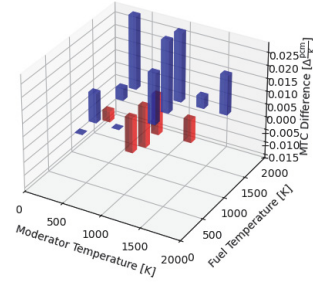
(a) Burnup=0 GWd/tHM



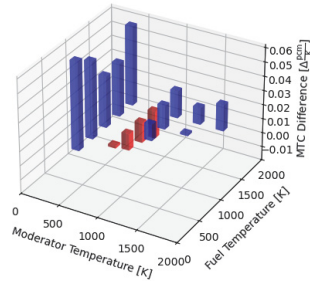
(b) Burnup=39.6 GWd/tHM



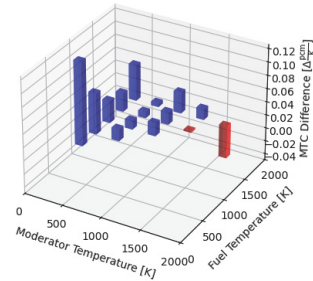
(c) Burnup=79.2 GWd/tHM



(d) Burnup=118.8 GWd/tHM

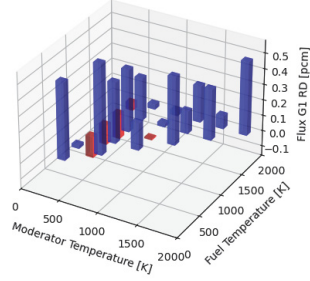


(e) Burnup=158.4 GWd/tHM

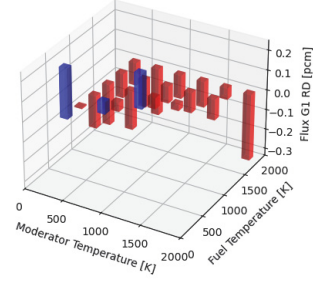


(f) Burnup=198.0 GWd/tHM

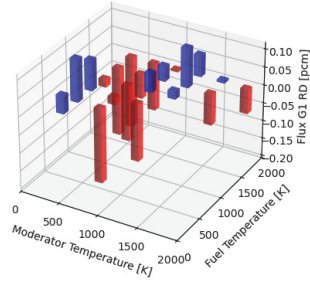
Figure 26. Simulated differences in the  $\overline{MTC}$  between ISOXML data and DNN for a homogeneous region consisting of 279 isotopes with number densities representative of a MOL PBR fuel pebble at the burnup of (a) 0 GWd/tHM, (b) 39.6 GWd/tHM, (c) 79.2 GWd/tHM, (d) 118.8 GWd/tHM, (e) 158.4 GWd/tHM, and (f) 198.0 GWd/tHM.



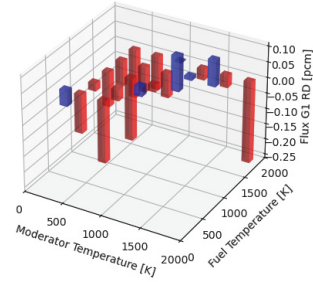
(a) Burnup=0 GWd/tHM



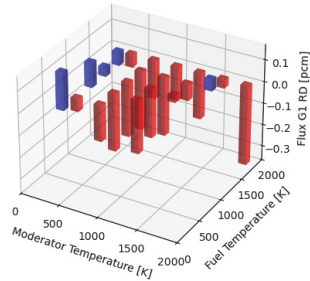
(b) Burnup=39.6 GWd/tHM



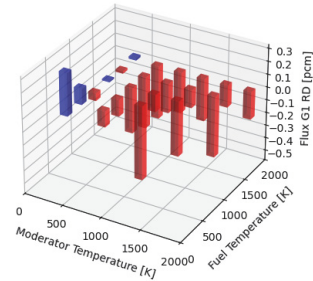
(c) Burnup=79.2 GWd/tHM



(d) Burnup=118.8 GWd/tHM

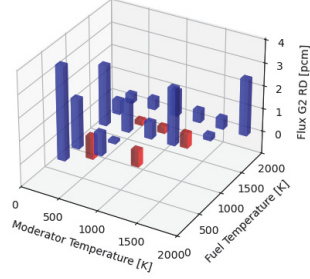


(e) Burnup=158.4 GWd/tHM

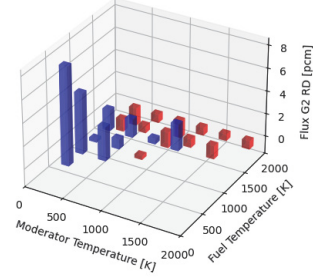


(f) Burnup=198.0 GWd/tHM

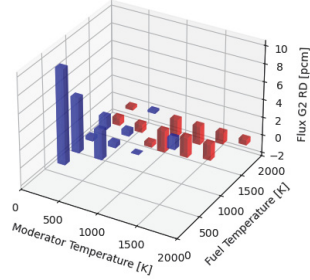
Figure 27. Simulated differences in the neutron flux for Energy Group 1 between ISOXML data and DNN for a homogeneous region consisting of 279 isotopes with number densities representative of a MOL PBR fuel pebble at the burnup of (a) 0 GWd/tHM, (b) 39.6 GWd/tHM, (c) 79.2 GWd/tHM, (d) 118.8 GWd/tHM, (e) 158.4 GWd/tHM, and (f) 198.0 GWd/tHM.



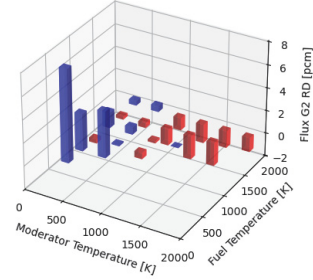
(a) Burnup=0 GWd/tHM



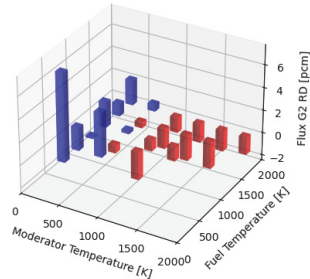
(b) Burnup=39.6 GWd/tHM



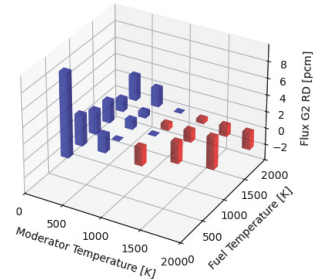
(c) Burnup=79.2 GWd/tHM



(d) Burnup=118.8 GWd/tHM

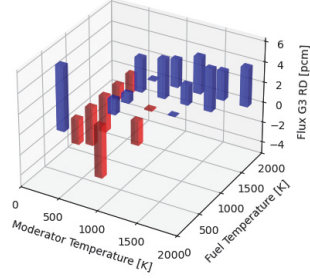


(e) Burnup=158.4 GWd/tHM

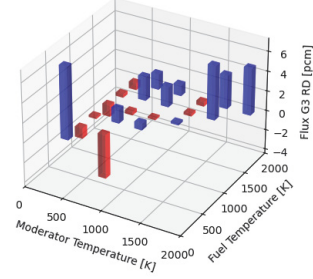


(f) Burnup=198.0 GWd/tHM

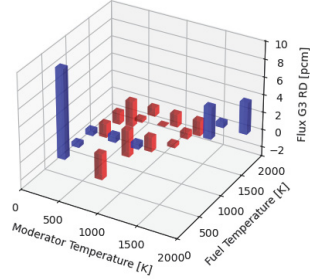
Figure 28. Simulated differences in the neutron flux for Energy Group 2 between ISOXML data and DNN for a homogeneous region consisting of 279 isotopes with number densities representative of a MOL PBR fuel pebble at the burnup of (a) 0 GWd/tHM, (b) 39.6 GWd/tHM, (c) 79.2 GWd/tHM, (d) 118.8 GWd/tHM, (e) 158.4 GWd/tHM, and (f) 198.0 GWd/tHM.



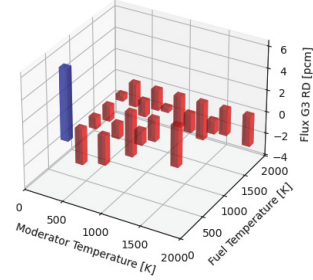
(a) Burnup=0 GWd/tHM



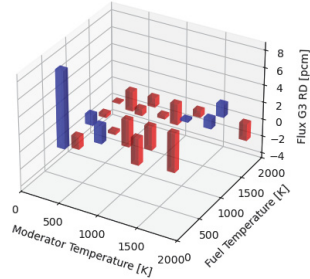
(b) Burnup=39.6 GWd/tHM



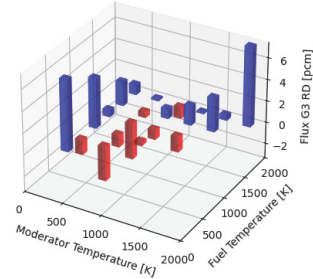
(c) Burnup=79.2 GWd/tHM



(d) Burnup=118.8 GWd/tHM



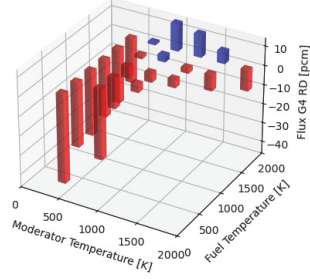
(e) Burnup=158.4 GWd/tHM



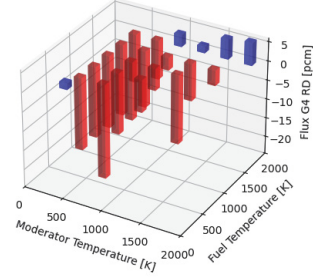
(f) Burnup=198.0 GWd/tHM

Figure 29. Simulated differences in the neutron flux for Energy Group 3 between ISOXML data and DNN for a homogeneous region consisting of 279 isotopes with number densities representative of a MOL PBR fuel pebble at the burnup of (a) 0 GWd/tHM, (b) 39.6 GWd/tHM, (c) 79.2 GWd/tHM, (d) 118.8 GWd/tHM, (e) 158.4 GWd/tHM, and (f) 198.0 GWd/tHM.

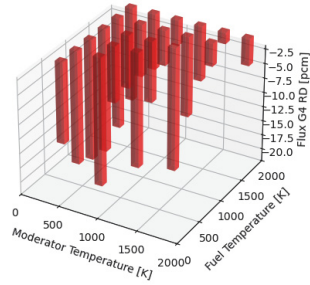




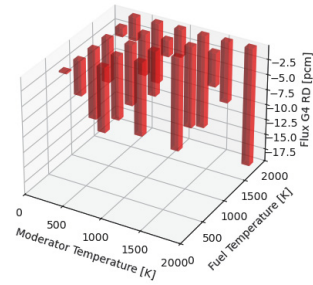
(a) Burnup=0 GWd/tHM



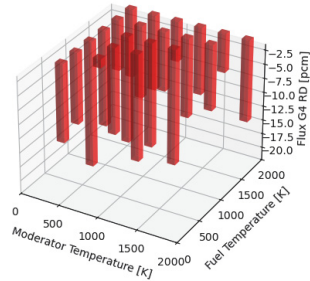
(b) Burnup=39.6 GWd/tHM



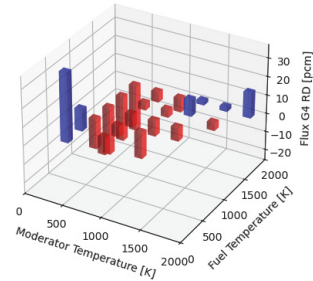
(c) Burnup=79.2 GWd/tHM



(d) Burnup=118.8 GWd/tHM



(e) Burnup=158.4 GWd/tHM



(f) Burnup=198.0 GWd/tHM

Figure 30. Simulated differences in the neutron flux for Energy Group 4 between ISOXML data and DNN for a homogeneous region consisting of 279 isotopes with number densities representative of a MOL PBR fuel pebble at the burnup of (a) 0 GWd/tHM, (b) 39.6 GWd/tHM, (c) 79.2 GWd/tHM, (d) 118.8 GWd/tHM, (e) 158.4 GWd/tHM, and (f) 198.0 GWd/tHM.